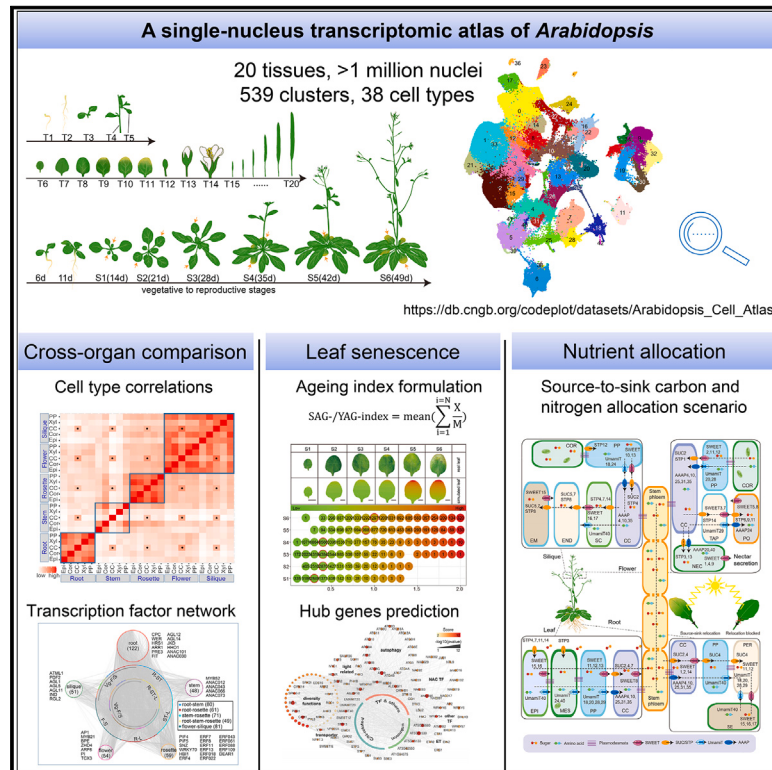


An *Arabidopsis* single-nucleus atlas decodes leaf senescence and nutrient allocation

Graphical abstract



Authors

Xing Guo, Yichuan Wang, Caiyao Zhao, ..., Huan Liu, Hongwei Guo, Xun Xu

Correspondence

liuhuan@genomics.cn (H.L.),
guohw@sustech.edu.cn (H.G.),
xuxun@genomics.cn (X.X.)

In brief

A comprehensive single-nucleus transcriptomic atlas of *Arabidopsis* across multiple tissues enables the quantification of leaf cell aging state at a single-cell level, highlighting the senescence-related hub genes and the construction of a nutrient allocation scenario among source leaves and sink organs.

Highlights

- Dynamic sampling across multiple tissues facilitated across-organ cell-type comparison
- Formulated SAG-index and YAG-index quantified leaf aging at the single-cell level
- Constructed gene regulatory network predicted key regulators in leaf senescence
- Mapped spectrum of C/N transporters illustrated the source-to-sink nutrient allocation



Article

An *Arabidopsis* single-nucleus atlas decodes leaf senescence and nutrient allocation

Xing Guo,^{1,12} Yichuan Wang,^{2,12} Caiyao Zhao,^{1,12} Cong Tan,^{3,12} Wei Yan,^{2,12} Sunhuan Xiang,³ Dan Zhang,² Hui Zhang,³ Mengting Zhang,^{3,4} Liujing Yang,^{3,5} Meng Yan,⁶ Pingli Xie,⁶ Yi Wang,⁶ Li Li,^{1,5} Dongming Fang,³ Xuanmin Guang,³ Wenwen Shao,^{1,5} Fang Wang,^{1,5} Haoxuan Wang,^{3,5} Sunil Kumar Sahu,^{1,3} Min Liu,³ Tong Wei,^{1,3} Yang Peng,² Yuping Qiu,² Tao Peng,² Yi Zhang,² Xuemei Ni,³ Zhicheng Xu,⁷ Haorong Lu,⁷ Zhonghai Li,⁸ Huanming Yang,³ Ertao Wang,⁹ Michael Lisby,¹⁰ Huan Liu,^{3,4,*} Hongwei Guo,^{2,*} and Xun Xu^{3,11,13,*}

¹BGI Research, Wuhan 430047, China

²New Cornerstone Science Laboratory, Institute of Plant and Food Science, Department of Biology, School of Life Sciences, Southern University of Science and Technology, Shenzhen 518055, China

³State Key Laboratory of Genome and Multi-omics Technologies, BGI Research, Shenzhen 518083, China

⁴BGI Life Science Joint Research Center, Northeast Forestry University, Harbin, Heilongjiang 150040, China

⁵College of Life Sciences, University of Chinese Academy of Sciences, Beijing 100049, China

⁶School of Agriculture, Yunnan University, Kunming 650500, China

⁷China National GeneBank, Shenzhen 518083, China

⁸State Key Laboratory of Tree Genetics and Breeding, College of Biological Sciences and Technology, Beijing Forestry University, Beijing 100083, China

⁹New Cornerstone Science Laboratory, Key Laboratory of Plant Carbon Capture, CAS Center for Excellence in Molecular Plant Sciences, Institute of Plant Physiology and Ecology, SIBS, Chinese Academy of Sciences, Shanghai 200032, China

¹⁰Department of Biology, University of Copenhagen, Copenhagen 2100, Denmark

¹¹Guangdong Provincial Key Laboratory of Genome Read and Write, Shenzhen 518083, China

¹²These authors contributed equally

¹³Lead contact

*Correspondence: liuhuan@genomics.cn (H.L.), guohw@sustech.edu.cn (H.G.), xuxun@genomics.cn (X.X.)

<https://doi.org/10.1016/j.cell.2025.03.024>

SUMMARY

With rapid advancements in single-cell RNA sequencing (scRNA-seq) technologies, exploration of the systemic coordination of critical physiological processes has entered a new era. Here, we generated a comprehensive *Arabidopsis* single-nucleus transcriptomic atlas using over 1 million nuclei from 20 tissues encompassing multiple developmental stages. Our analyses identified cell types that have not been characterized in previous single-protoplast studies and revealed cell-type conservation and specificity across different organs. Through time-resolved sampling, we revealed highly coordinated onset and progression of senescence among the major leaf cell types. We originally formulated two molecular indexes to quantify the aging state of leaf cells at single-cell resolution. Additionally, facilitated by weighted gene co-expression network analysis, we identified hundreds of promising hub genes that may integratively regulate leaf senescence. Inspired by the functional validation of identified hub genes, we built a systemic scenario of carbon and nitrogen allocation among different cell types from source leaves to sink organs.

INTRODUCTION

Senescence and nutrient reallocation are critical processes for plant development, reproduction, and acclimation to environmental stresses. As autotrophic organisms, plants recycle their components to support the development of sink organs, such as roots, stems, flowers, and siliques, through leaf senescence.¹ This process requires intricate spatiotemporal coordination of various cell types and the precise regulation of key functional genes. The ability to track these dynamic processes at the single-cell level is essential for understanding the molecular mechanisms that govern senescence and nutrient redistribution across different organs.

The recent development and widespread use of high-throughput single-cell RNA-seq (scRNA-seq) technology have significantly advanced the identification and characterization of plant cell types at the single-cell transcriptomic level. Numerous single-cell atlases for individual organs have been constructed over the past 6 years (Table S1), most of which rely on protoplasting. However, studying leaf senescence and nutrient reallocation at single-cell resolution remains challenging due to the difficulties in isolating protoplasts from senescing leaves, as well as from flowers and fruits, which are critical sink organs for nutrient redistribution.

In recent years, single-nucleus RNA sequencing (snRNA-seq), which does not rely on protoplasting, has been widely applied in



various plant tissues (Table S1). It allows nuclei isolation from samples of multiple tissue types or successive developmental stages.^{2–6} Large-scale analyses integrating multiple tissues based on snRNA-seq are emerging. For instance, an *Arabidopsis* seed-to-seed atlas using 800,000 nuclei⁷ and two soybean atlases sampling across ten tissues^{8,9} demonstrated the feasibility of snRNA-seq in generating a comprehensive cell atlas. These large-scale projects have provided a solid foundation for understanding transcriptional regulation across different plant tissues. Building on these advancements, the integration of snRNA-seq for studying leaf senescence and source-to-sink nutrient dynamics at the single-cell level offers a unique opportunity to uncover the molecular networks that drive leaf senescence and nutrient reallocation.

Here, we constructed a comprehensive single-nucleus transcriptomic atlas of *Arabidopsis* encompassing multiple developmental stages of major organs to explore the interplays between cellular identity, transcriptional regulation, and physiological function. By leveraging time-resolved sampling and integrative analyses, we have developed and validated two molecular indexes for quantifying aging states at the single-cell resolution and uncovered the transcriptional networks and key factors driving leaf senescence and source-to-sink nutrient dynamics. Our atlas also contributes a fundamental single-cell transcriptomic reference for future functional studies in plants.

RESULTS

Generation of a comprehensive *Arabidopsis* single-nucleus atlas

A total of 20 tissues that represent the key developmental stages and transitions throughout the entire life cycle were collected (sampling strategy was provided in STAR Methods) (Figure 1A; Table S1). The snRNA-seq data was generated based on a universal fluorescence-activated cell sorting (FACS)-free nuclei isolation protocol¹⁰ and DNBelab C Series Single-Cell Library Prep Set (MGI, 1000021082) as previously described.¹¹ Over one million nuclei passed the standardized filtering criteria with >200 genes per nucleus. Following the majority of previous studies (Table S1), we used a more rigorous criterion with >500 genes per nucleus to obtain high-quality nuclei for downstream analyses. A total of 913,769 nuclei passed our quality control, with 1,610 mean genes and 2,451 mean unique molecular identifiers (UMIs) captured in each nucleus (Figure 1B; Table S1).

Cells from each of the 20 tissues were both independently clustered to generate single-tissue atlases (Figures S1 and S2; Table S1) and integrated as a comprehensive integrative atlas (Figures 1C, 1D, and S2U). Independent clustering of each dataset resulted in a total of 539 clusters, 96.5% (520 out of 539) of which were successfully annotated to corresponding cell types based on known cell-type marker genes or biological functions of cluster-enriched genes (Figures 1E, S1, and S2; Table S1). In a global view of the integrative uniform manifold approximation and projection (UMAP) plot, cells of roots, shoots, stems, and leaves were located at the bottom left, while cells of flowers and siliques were assigned at the top right (Figure 1C), suggesting a high divergence of transcriptome spectrum between vegetative and reproductive organs. The distant distribution of root

cells to cells of other vegetative organs also implied high heterogeneity between the ground organs and aerial organs (Figure 1C). In the integrative UMAP plot, a total of 43 clusters revealed 25 major cell types, corresponding to the known identities that were validated by histological and single-cell studies in *Arabidopsis* (Figure 1D; Table S1). Interestingly, we found two companion cell (CC) clusters (C6 and C38) that both consisted of cells from all the collected organs. Similar patterns were also detected for the guard cell (GC; C11). The ground cells from different organs were grouped into several adjacent clusters (C0, C1, C3, C4, C12, C21, C29, and C33) (Figure 1D). These clustering patterns suggested that the cell-type identification using single-nucleus transcriptomic data was unaffected by batch effects from different tissues.

Taken together, we identified at least 38 cell types by integrating annotation of the 20 tissues and the combined organ-level datasets. There were 11 cell types shared in multiple organs, which were defined as common cell types, such as epidermis (EPI), mesophyll (MES), cortex (COR), and vascular (VAS) cell (Figure 1E), suggesting essential roles of these cell types for sustaining basic growth of each organ. We also defined several organ-specific cell types (Figure 1E) that correspond to the specific biological roles of each organ.

Intra-organ integration and cross-organ comparison

Our samples covered root, stem, shoot, leaf, flower, and silique, allowing comprehensive cell-type annotation for each organ (Figures 2A–2G and S3A–S3P) and cross-organ comparison (Figures 2H–2K). Benefiting from the multi-stage sampling strategy and integrative clustering, we generated a cell landscape for each organ and annotated the hidden cell types that were missed in the single-sample analysis (Figures 2, S1, and S2). In roots, we identified 13 cell types (Figures S1A, S1B, S2A, S2B, and S3A) that were highly consistent with previous single-cell studies.^{12–16} The suberized endodermis (supported by glycerol-3-phosphate acyltransferase 5 [GPAT5], Figure S3C) that had not been reported yet in previous protoplasting-based single-cell studies^{14–16} was also identified in our data (Figure S3D) and another snRNA-seq data generated from primary roots,¹² demonstrating the advantage of the single-nucleus approach in mature tissues over protoplasting. We also performed a cross-validation between our 6-day root data and the published 7-day root data¹² and confirmed that the annotation of each cell type was well matched (Figures S3E and S3F). These results highlighted the high quality and reliability of snRNA-seq root data in this study. Notably, through pseudotime trajectory analysis and a comparison with published root cortex clusters harboring developmental stage information,¹⁶ we found that the six cortex clusters identified in our 6-day-old root belonged to different spatial regions of the roots, as also demonstrated by the dynamic expression of cortex marker genes and the changes of enriched biological processes (Figures S1A, S2A, and S3G–S3J; Table S1).

Stem is essential in providing support and transporting water and nutrients between other organs.¹⁷ Consistent with a recent snRNA-seq atlas by Lee et al.,⁷ we identified almost all known cell types in stem (Figures 2A, S1D, and S2D; Table S1). However, no well-known markers were detected in cluster 0 that is

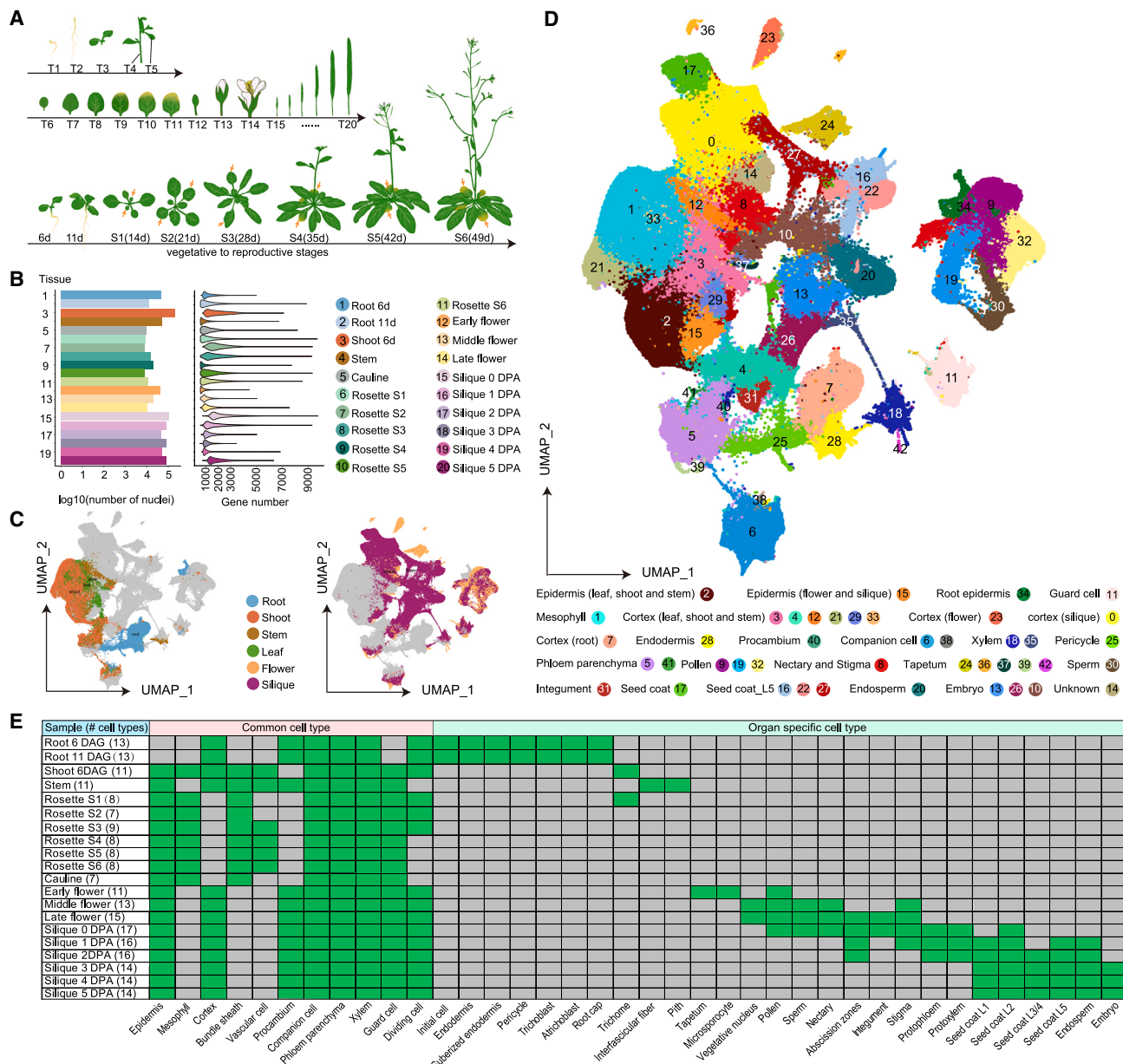


Figure 1. A comprehensive single-nucleus atlas of *Arabidopsis*

(A) Schematic illustration of the sampling strategy in this study. A total of 20 tissues (T1-T20) were collected from vegetative growth to reproductive growth, with six stages of the second pair of true leaves indicated by arrows.

(B) Numbers of profiled nuclei and captured genes of each sample.

(C) UMAP of global clustering of all cells colored by organs.

(D) UMAP of single-nucleus atlas of *Arabidopsis* colored by major cell types.

(E) Summary of all cell types that identified in the 20 tissues.

See also Figures S1 and S2.

located at the center of the UMAP plot. We therefore utilized Stereo-seq¹⁸ to compensate our cluster annotations. By mapping each snRNA cluster to Stereo-seq data, we observed that the majority of cell types matched well between the two methods (Figure 2B), such as CC (C8). C0 mainly located at the center of the cross section of stem, suggesting it is likely pith cell. We

also identified several *de novo* marker genes for pith cell (Figure S3K).

In shoots and rosettes, the largest proportion of cells we identified was MES (Figures 2C, S3L, and S3M). It is notable that trichome (supported by well-known trichome-specific markers GLABRA2 [GL2], long-chain acyl-CoA synthetase [LACS1], and

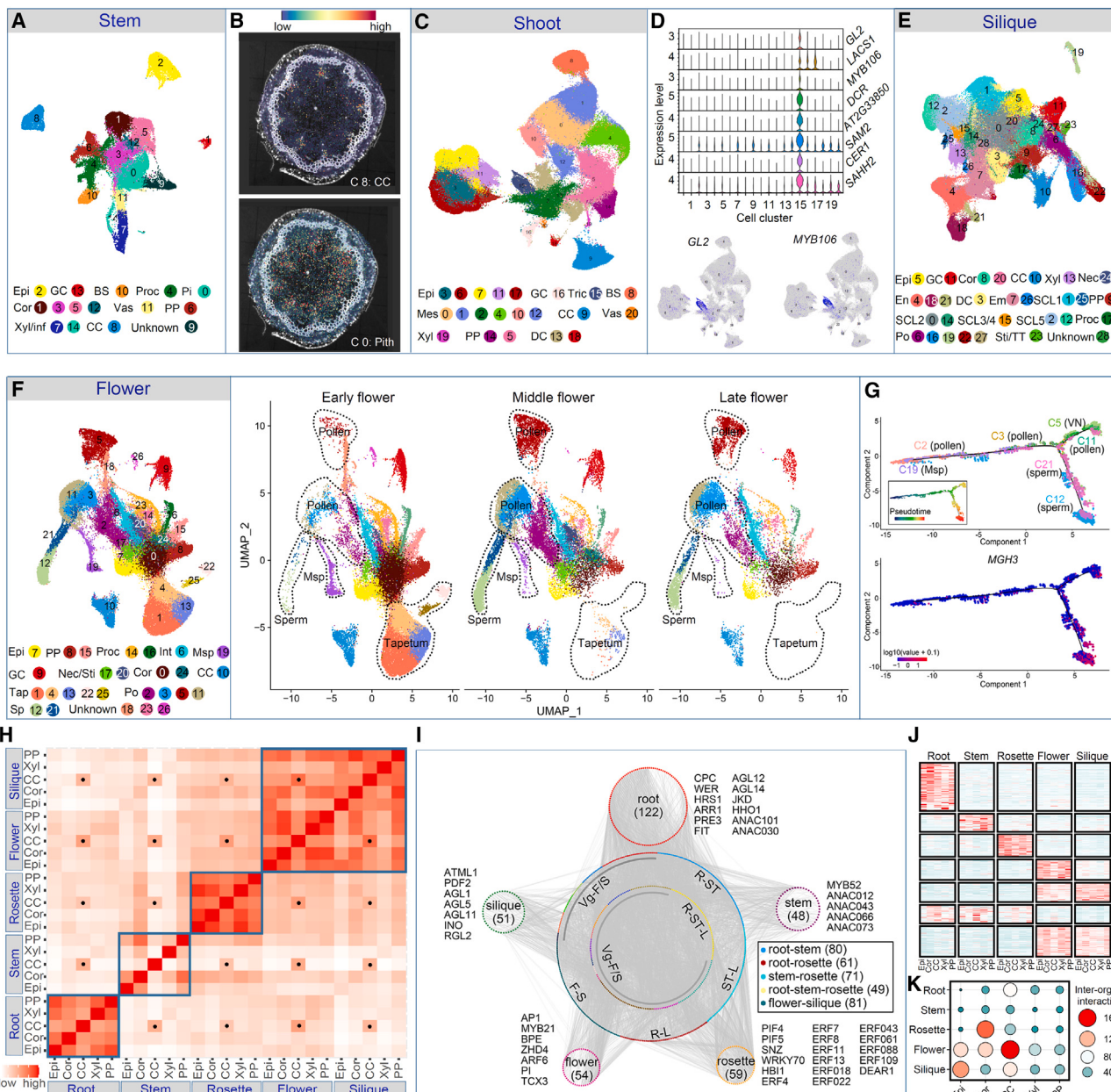


Figure 2. Integrative cell-type characterization and cross-organ comparison

- (A) Cell clusters and annotation of stem.
- (B) Validation of clusters by spatial transcriptomes in stem.
- (C) Cell clusters and annotation of shoot (6 days after germination [DAG]).
- (D) Expression specificity of trichome marker genes in shoot (6 DAG).
- (E) Integrative cell clusters and annotation of six stages of siliques (0–5 days post anthesis [DPA]).
- (F) Integrative cell clusters, annotation, and dynamic changes of cell composition in three stages of flowers.
- (G) Pseudotime trajectory analysis of pollen development. The sperm-specific gene *MGH3* was plotted on the pseudotime trajectory.
- (H) Pairwise correlation of average gene expression levels among the selected cell types across the five major organs.
- (I) Co-expression network of enriched TFs at the organ level.
- (J) Heatmap of enriched TFs in each organ and across organs.
- (K) Co-expression interactions of TFs for each cell type across the five major organs.

Abbreviations for cell types: Epi, epidermis; GC, guard cell; BS, bundle sheath; Proc, procambium; Cor, cortex; PP, phloem parenchyma; Vas, vascular cell; Xyl, xylem; CC, companion cell; Inf, interfascicular fiber; Tric, trichome; Mes, mesophyll; DC, dividing cell; Nec, nectary; En, endosperm; SC, seed coat; Em, embryo; Sti, stigma; TT, transmitting tract; Int, integument; Msp, microsporocyte; Tap, tapetum; Sp, sperm; PER, pericycle; Pl, pith; PO, pollen; EN, endosperm; Atr, atrichoblast; End, endodermis; SE, suberized endodermis; IC, initial cell; RC, root cap; Tri, trichoblast.

See also [Figure S3](#).

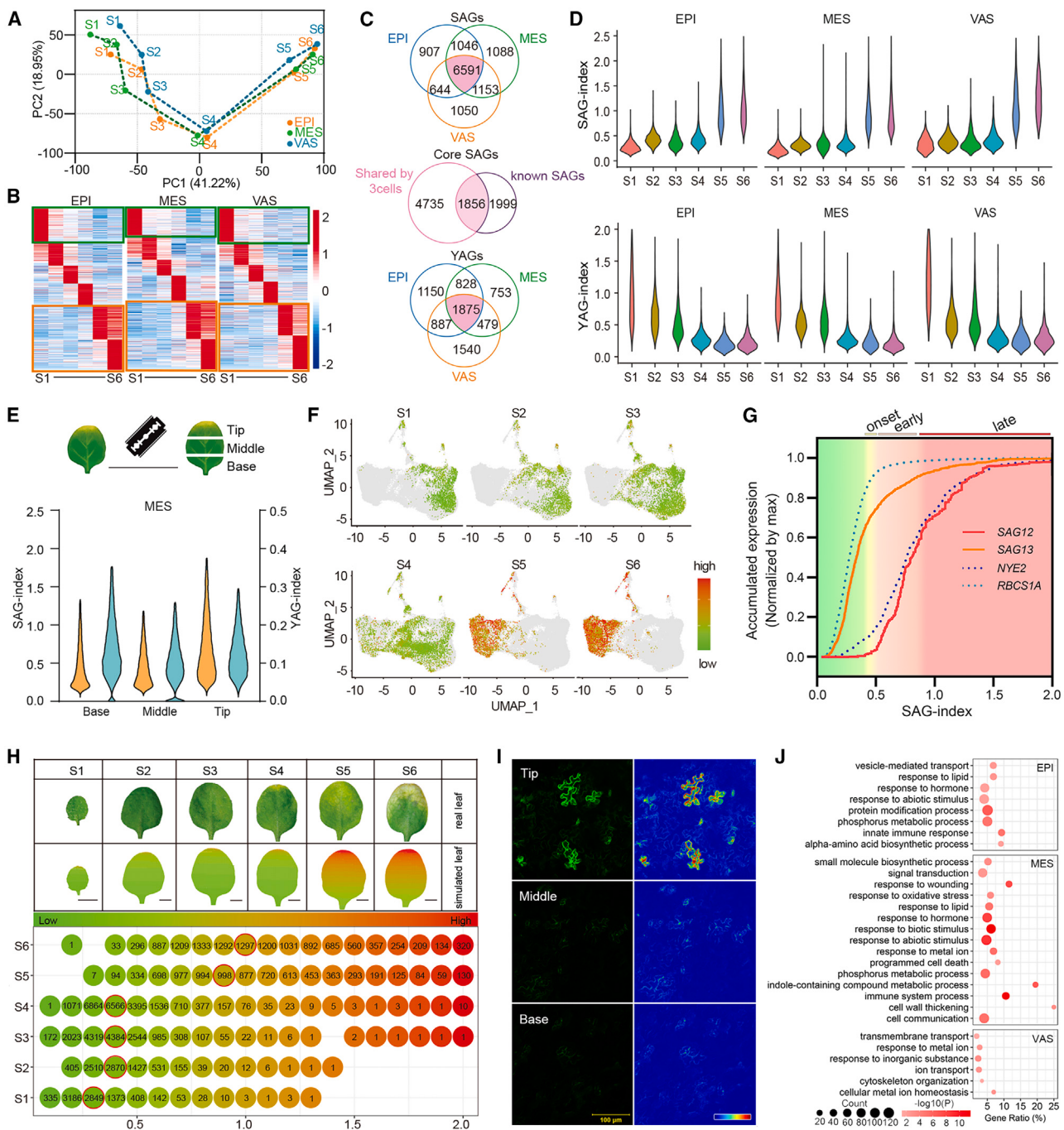


Figure 3. Quantitative measurement of single-cell aging state in leaf by SAG-index and YAG-index

- (A) PCA plot of cell-type-specific transcriptomes along six sampling stages of rosette leaves.
- (B) Heatmap showing expression patterns of genes in EPI, MES, and VAS cells along sampling stages. Genes with relatively higher expressions at early (S1) or late stages (S5-S6) in the three major cell types are marked with green and orange boxes respectively. The scale bar represents the normalized expressions by Z score.
- (C) Venn diagrams showing the identification of core senescence-associated genes (core SAGs) and youth-associated genes (YAGs).
- (D) Distributions of SAG-index and YAG-index values in the three major cell types along sampling stages.
- (E) Distributions of SAG-index and YAG-index in MES cells located in base, middle, and tip segments of S4 rosette leaves. Orange, SAG-index; cyan, YAG-index.
- (F) Dynamic changes of SAG-index in all the leaf cells along the six sampling stages. Relative SAG-index values are indicated by the color bar.
- (G) Accumulated expressions of SAG12, SAG13, NYE2, and RBCS1A along the SAG-index in MES cells. According to the kinetics of accumulation curves, SAG-index ranges were assigned with different stages of leaf development as indicated above the plot.

(legend continued on next page)

myeloblastosis transcription factor 106 [MYB106]), which has not been identified in previous protoplasting-based single-cell studies, was detected in our shoot (Figure 2C) and young rosette (Figures S1F and S2F). We also identified multiple *de novo* markers for trichome (Figure 2D; Table S1). The detection of trichome cells in our study and a recent multi-organ single-nucleus atlas⁷ demonstrated the advantage of snRNA-seq in resolving recalcitrant tissues and more comprehensive characterization of cell types across organs.

In reproductive organs, siliques and flower (Figures 2E, 2F, and S3N–S3P), besides the common cell types, we also defined many tissue-specific cell types, such as seed coat, embryo, and endosperm in siliques (Figure 1E) and microsporocyte, pollen, tapetum, and sperm in flowers (Figure 1E). The identification of these tissue-specific cell types in flower and siliques demonstrated the robustness of our atlas and high resolution of annotation. Notably, we found the detectable endosperm seemed to be 3–4 days earlier than embryo, although the double fertilization occurred almost simultaneously (Figures S3N and S3O; Table S1). The microsporocyte and tapetum were largely detected in early flower but not in middle and later flower (Figures 2F, 2G, S1L–S1N, and S2L–S2N), consistent with the development of microsporocyte and degradation of tapetum during flowering.¹⁹ On the contrary, the pollen grains and sperm cells were in low abundance in early flower and reached their peak in middle flower. Trajectory analysis implied that the pollen grains were derived from microsporocyte and eventually developed into sperm and vegetative nucleus (VN), as indicated by the sperm-specific gene *male gamete-specific histone H3* (MGH3) and VN-enriched genes class XI myosin D (*XID*) and *LURE pollen tube attractant 1* (*LURE1*),²⁰ respectively (Figures 2G and S3Q).

How multiple function-specialized organs and cell types cooperate to ensure the proper development and growth of the whole plant has not been well estimated. We proposed that the differences in regulatory network are involved in the functional specialization of organs and cell types, while certain major regulators could coordinate the processes among them. We therefore performed a pairwise comparison among the five major cell types from root, stem, rosette, flower, and siliques to unveil general features at both organ and cell-type levels during plant development. The relatively higher correlation coefficients among cell types within each organ than cell pairs across organs (Figures 2H and S3R) indicated general high inter-organ cell heterogeneity, which was also supported by the numerous organ-enriched transcription factors (TFs) (Figures 2I–2K). There were more TFs that showed predominant expressions in root, including the well-known genes *CAPRICE* (*CPC*) and *WEREWOLF* (*WER*).²¹ NAC-domain-containing TFs that are related to secondary cell wall

thickening²² were highly expressed in the stem, while genes encoding ethylene response factors (ERFs) were enriched in the rosette, consistent with the structural support function of stem²³ and stress-responsive function of rosette.²⁴

Unexpectedly, we found the highest expression diversity in stem cells than other organs, indicating high differentiation and functional specialization of stem cells (Figures 2H and 2K). On the contrary, relatively higher similarities and more common TFs were observed among the cell types of reproductive organs flower and siliques than those of vegetative organs (Figures 2H, 2K, S3T, and S3U), probably due to developmental continuity during flower-to-fruit transition. Besides the functional specialization-related organ-specific TFs, we also identified numerous common TFs presented in both vegetative and reproductive organs, which may cooperatively regulate the development, growth and environmental adaptation of whole plants, such as the well-known homeodomain protein GL2 that affects epidermal cell identity in trichome, root hair and seed coat,²⁵ the growth-regulating factor 1 (GRF1) that functions in balancing growth and stress responses in root, shoot, and flowers²⁶ and the lateral organ polarity transcriptional repressor KANADI 1 (KAN1) that regulates lateral root formation and development, and abaxial identity in leaf, carpel and the outer integument of ovule²⁷ (Figure 2I; Table S1).

Despite the high inter-organ divergence among the major cell types, we found a remarkable similarity in CCs and GCs among different organs (Figures 2H, 2K, and S3R), which might be correlated with the highly conserved function of CCs and GCs across the whole plant,²⁸ as reported by Lee et al.⁷ The organ- and cell-type-level expression profiles and TF landscape may serve as important sources for uncovering the functional differentiation and cooperation among different organs and cell types.

Quantification of leaf senescence at single-cell level

The progressive growth and senescence of leaves are tightly regulated by hierarchical expressions of thousands of senescence-associated genes (SAGs).^{29–31} Recent single-cell transcriptomics studies have revealed functional divergence among different leaf cell types,^{28,32} but how different cell types coordinate during leaf senescence at single-cell level remains unclear.

To identify both common and cell-type-specific transcriptional features during leaf expansion and senescence, we first conducted a principal-component analysis (PCA) of the transcriptomes of the three major leaf cell types, including EPI (without GCs), MES, and VAS (including both phloem- and xylem-related cell types), along the six sampling stages (S1–S6) (Figure 3A). Interestingly, the sampling stage, rather than cell type, was the first principal component (Figure 3A). Furthermore, the three cell types tended to cluster more densely as the aging

(H) Simulated leaves and cell alignment based on the SAG-index values of all the leaf cells along the six sampling stages. Cells with various SAG-index were counted for each stage, with 0.1 as the step size. Numbers in dots indicate the counts of cells with indicated SAG-index value. Red circles mark the cell population with median SAG-index value of each sampling stage. Scale bar, 5 mm.

(I) Confocal images of the *RPGE2pro::RPGE2-GFP/Col-0* marker line at S3 stage, representing putative early senescent leaf cells. Scale bar, 100 μm; relative intensity of GFP signals were encoded by a pseudo-color scale bar. Similar distributions of GFP-labeled cells were observed in five individual plants.

(J) Biological GO enrichment of genes differentially expressed in the cells with top 5% high SAG-index values, compared with cells with median SAG-index values (45%–55%).

See also Figure S4.

progressed with a clear transition at stage 4 (S4) (Figure 3A). These results strongly suggested tight coordination of both the onset and progression of senescence among the three cell types. Similar cell-type-independent transcriptional changes during leaf aging were also noted by Lee et al.⁷ To further explore important genes involved in such coordination, cell type-enriched SAGs that were highly expressed at the last two sampling stages were identified (see STAR Methods, Figures 3B and S4A–S4C, and Table S2). Of these SAGs, 6,591 were common among the three major cell types (Figure 3C; Table S2), including 1,856 core SAGs that overlapped with previously published SAGs³¹ (known SAGs) (Figure 3C; Table S2). Additionally, we also identified 1,875 common youth-associated genes (YAGs) that expressed higher during the early expansion stage (S1) (see STAR Methods, Figures 3B, 3C, and S4A–S4C, and Table S2).

The basipetal yellowing of leaves during senescence implies a large heterogeneity of cellular states and transcriptomes among leaf cells.³⁰ To quantify such heterogeneity at single-cell level, we formulated SAG-index and YAG-index using core SAGs and YAGs (see STAR Methods). As expected, the YAG-index peaked at early leaf expansion stage (S1) and gradually decreased during development, while SAG-index remained low until it dramatically increased after the appearance of yellowish tips on the leaf (S5–S6) (Figure 3D). Validation using snRNA-seq data from physically dissected S4 leaf fragments further confirmed the accuracy of these two indexes: the yellow leaf tip fragments exhibited the highest SAG-index and the lowest YAG-index, reflecting visible senescence (Figures 3E and S4D). Moreover, by employing homologous genes of *Arabidopsis* SAGs and YAGs in *Populus*, we demonstrated that the SAG-index and YAG-index together can reliably quantify aging state of leaf cells not only in *Arabidopsis* but also in other dicotyledonous species (Figures S4E–S4H). We also tested both indexes with previously published bulked mRNA-seq data of various tissues that were sampled with developmental stages, including root, stigma, and embryo (Figure S4I; Table S2), as well as our root snRNA-seq data (Figures S4L–S4N), all of which verified that the two indexes together could also be used to quantitatively estimate the developmental states of these organs.

To further illustrate the dynamic heterogeneity of cellular states during leaf development, both SAG-index and YAG-index were plotted on the integrative rosette UMAP (Figures 3F and S4O). Strikingly, cells from the six successive sampling stages showed a progressive right-to-left distribution on the UMAP, with S4 cells evenly distributed and bridged the early stages (S1–S3) and late stages (S5–S6) (Figures 3F and S4O), implicating the onset of transcriptional transition at S4. By examining the accumulated expressions of genes associated with carbon fixation (*RBCS1A*) and chlorophyll breakdown (*NYE2*), as well as two classic markers of early-stage (SAG13) and late-stage (SAG12) senescence, we have further confirmed that SAG-index values of single nuclei aligned well with the sequential physiological events of leaf senescence (Figure 3G).

Based on spatial-temporal changes of SAG index during leaf senescence (Figures 3D, 3E, and S4D), we simulated the senescence progression of leaves by arranging cells with gradually decreasing SAG-index from the tip to the base of each leaf (Figure 3H). Interestingly, the simulated leaves highly resembled the

basipetal yellowing phenotype of the real leaves (Figure 3H), indicating that SAG-index is indeed a good measurement of leaf cell aging state. Unexpectedly, even in the completely green S3 leaf, many cells harbored relative higher SAG-index values (Figures 3F–3H), and cells with relative higher YAG-index values were also dispersed in the late senescing S6 leaf (Figure S4O). We speculated that cells with relatively higher SAG-index in the visually green S3 may collectively trigger the leaf-level senescence. To locate these putative early senescing cells, we have identified SAGs highly expressed in the 5% of S3 leaf cells with higher SAG-index values and generated transgenic marker lines that express GFP-fused SAG proteins under their native promoters (see STAR Methods, Figure S4P, and Table S2). As illuminated by the *RPGE2pro::RPGE2-GFP/Col-0* marker line, putative senescing cells were scatteredly distributed over the leaf blade and prone to locate in the tip segmentation of S3 leaves (Figure 3I). We also found that the cells with top 5% SAG-index in S3 leaves were highly enriched in stress response and immunity-related processes (see STAR Methods, Figure 3J, and Table S2). These results indicated that local stresses together with leaf cell age may contribute to the heterogeneous initiation of senescence in the leaf tip. Corresponding to this observation, we have also verified with published bulked RNA-seq data that multiple biotic and abiotic stresses lead to higher values of SAG-index and lower values of YAG-index (Figures S4J and S4K).

Despite the global inter-cell-type coordination (Figures 3F, 3H, and S4O), whether the onset and progression of senescence among the three major cell types are completely synchronized remains unclear. We therefore conducted pseudotime analysis of each major cell type and equally divided the pseudotime into 10 bins (T0 to T9). As expected, SAG-index progressively increased along the pseudotime of each cell type, opposite to YAG-index (Figures S4Q and S4R). By tracing the origin of sampling stage for each cell type, we found obvious overlapping occupation of pseudotime between sampling stages, reflecting progressive and continuous change of single-nucleus transcriptome over the six successive sampling stages (Figure S4S). Moreover, we noticed distinct pseudotime distribution patterns among the three major cell types (Figure S4S), suggesting differential transcriptional dynamics among them. Interestingly, Gene Ontology (GO) enrichment analysis of cells at the turning points at S4 for each cell type also supported the prominent roles of stress response and immunity-related processes on triggering aging state transition (Figure S4T).

Cauline leaves, as another major photosynthetic organ that protects emerging floral buds and contributes nutrients during seed filling and maturation, may play similar roles as rosette leaves for nutrient recycling during leaf senescence.^{1,33,34} To test this hypothesis, we compared the gene expression profiles of cauline leaves at 42 days with those of rosette leaves (S1–S6). Our results revealed a high degree of similarity between cauline leaves and rosette leaves at the S2 and S3 stages, in global gene expression (Figure S4U) and genes related to carbon and nitrogen pathways (Figure S4V), as well as core SAGs and YAGs (Figure S4V; Table S2). This similarity indicates that cauline and rosette leaves indeed undergo comparable senescence and nutrient allocation processes.

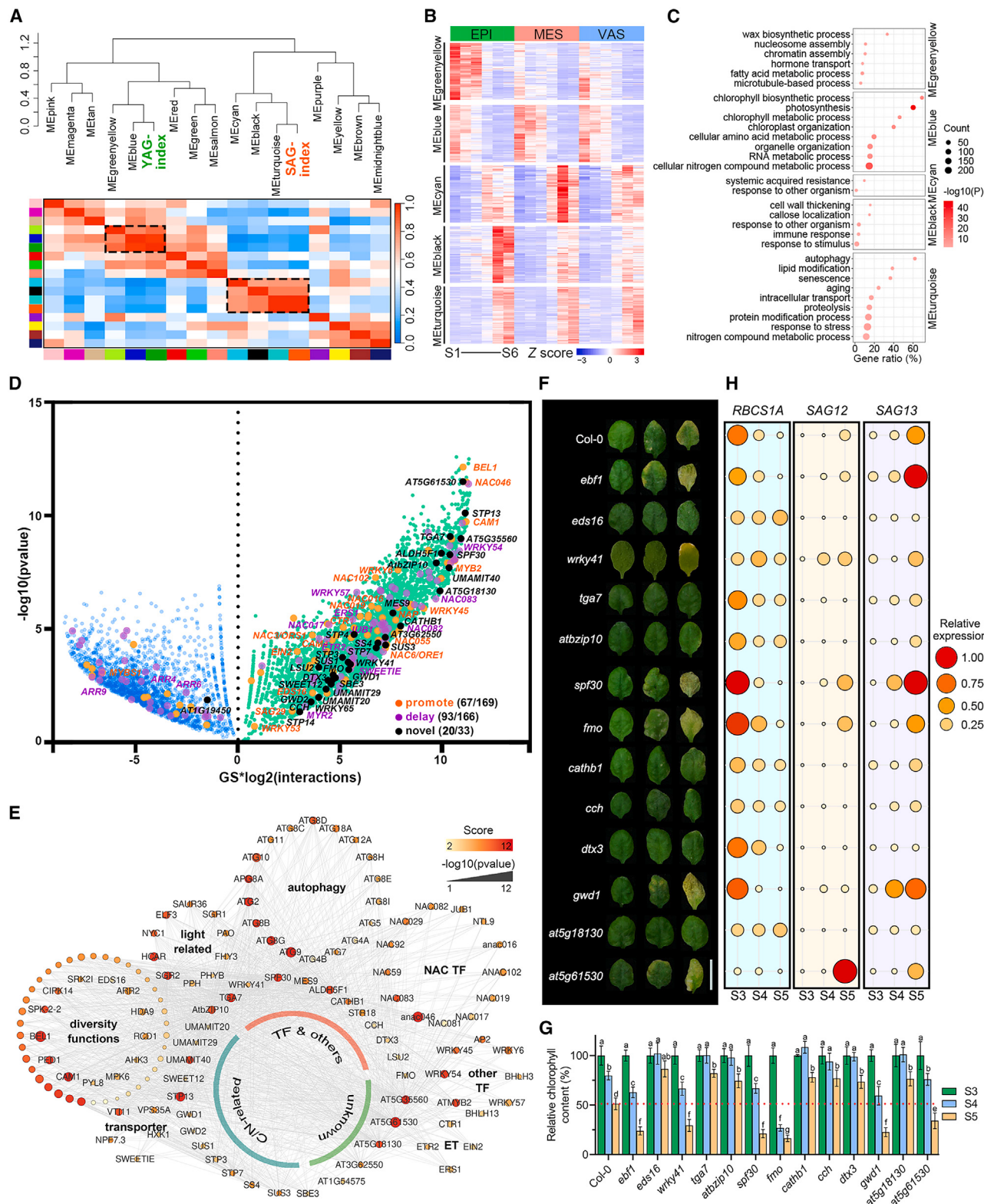


Figure 4. Identification of promising senescence-associated hub genes

(A) Identification of co-expression modules with SAG-index or YAG-index in EPI, MES, and VAS cells with WGCNA. Modules that showed high Pearson's correlations with SAG-index or YAG-index are marked with dashed boxes.

(legend continued on next page)

Identification of promising hub SAGs by co-expression analysis

Although hundreds of known SAGs have been functionally studied,³¹ how they regulate leaf senescence at single-cell level is largely unclear. Moreover, identification of unreported SAGs will benefit the decryption of the mystery of plant senescence. Taking advantage of snRNA-seq of leaves from multiple developmental stages, we were able to comprehensively identify unreported hub SAGs. Genes that showed high correlations with either YAG-index or SAG-index in EPI, MES, and VAS cells were classified into five modules through weighted gene co-expression network analysis (WGCNA) (Figure 4A; Table S2). As expected, genes closely correlated with YAG-index were highly expressed at early stages and mostly decreased at S4, while genes correlated with SAG-index were gradually increased in expression along the sampling stages (Figure 4B). The two modules positively correlated with YAG-index were highly expressed at early stages and significantly enriched in growth-related GO terms, such as photosynthesis, chlorophyll biogenesis and metabolic processes, hormone transport, chromatin, and nucleosome assembly (Figure 4C). On the contrary, modules positively correlated with SAG-index were increased in expression along the sampling stages and enriched in autophagy, aging, and senescence, responding to stress-related GO terms (Figure 4C).

Compared with the 335 functionally validated SAGs,³¹ 47.76% known senescence-promoting (67/169) or -delaying (93/166) regulators were presented in the two modules (MEturquoise and MEblue) that showed the highest correlations with either YAG index or SAG index, respectively, indicating the high accuracy of our analysis (Figure 4D). To comprehensively identify promising hub SAGs, we estimated the correlations of genes with SAG index (see STAR Methods). As shown in Figure 4D, most of the known SAGs showed significant correlations with SAG index, including multiple genes belonging to NAC and WRKY DNA-BINDING PROTEIN (WRKY) TF families¹ and genes related to autophagy³⁵ and ethylene signaling.^{1,31,36}

To estimate the accuracy of the identified hub genes and their correlations with leaf senescence, we selected 22 hub genes with varied scores and estimated their co-expressions with functionally studied SAGs (Figure 4D; Table S2). Strikingly, these selected genes showed high co-expressions with functionally validated SAGs (Figure 4E), especially SAGs related to autophagy, light-harvesting, and chlorophyll breakdown, and TFs belong to NAC, WRKY, and basic helix-loop-helix (bHLH) families; ethylene signaling; and carbon/nitrogen transporters. We then obtained T-DNA insertion mutants of the 22 selected genes and evaluated their dynamic senescence phenotypes at multiple

levels (Table S2). Compared with the wild-type Col-0, the known early-senescence mutant *ebf1*³⁷ and delayed-senescence mutant *eds16*³⁸ we found that the mutants of 11 genes (50%) showed altered senescence onset and progression indicated by leaf color and chlorophyll content changes (Figures 4F and 4G). Moreover, mutants with delayed leaf senescence also showed delayed and lower expressions of *SAG12* and *SAG13* and prolonged expression of *RBCS1A*,^{39,40} while mutants with earlier senescence phenotypes showed the opposite trend (Figure 4H). Taken together, these observations have demonstrated the high efficiency and accuracy of exploiting SAG index in the detection of promising leaf-senescence regulating genes, and the large amounts of unstudied hub genes we identified may serve as valuable senescence-associated candidates for more detailed investigations.

A further survey of corresponding gene functions for the mutants with altered senescence phenotype indicated a complex and multifaceted regulation of leaf senescence. *WRKY41* (*AT4G11070*) and *WRKY65* (*AT1G29280*) encode two TFs that showed gradually increased expression levels along the sampling stages, with *WRKY41* expressed significantly higher than *WRKY65* (Figure S5A). Additionally, *WRKY41* was highly co-expressed with known autophagy-related factors and NAC TFs, much more than *WRKY65* (Figure S5B). We observed promoted senescence only in the *wrky41* mutant (Figures 4F–4H). Similarly, both TGACG SEQUENCE-SPECIFIC BINDING PROTEIN 7 (*TGA7*) and *Arabidopsis thaliana* basic leucine zipper 10 (*AtbZIP10*) were highly co-expressed with known SAGs, and null mutation of either gene significantly delayed senescence (Figures 4F–4H and S5B).

Besides TFs, we also found several genes with diverse biological functions correlated with leaf senescence, including the SPLICING FACTOR 30 (SPF30) encoding gene (*AT2G02570*), an auxin biosynthesis-related YUCCA family gene *FMO* (*AT1G12200*), cathepsin B-like protease encoding gene (*CATHB1*, *AT1G02300*), and the gene encoding COPPER CHAPERONE (*AT3G56240*, *CCH*), as well as a starch degradation-related gene *GWD1*⁴¹ (*AT1G10760*) and two unknown function genes *AT5G61530* and *AT1G61530* (Figure 4F–4H). We found promoted leaf senescence in the *spf30* mutant, further supporting the regulation of alternative splicing on ageing in plants.^{42,43} *FMO* encodes a flavin monooxygenase that essential for indole-3-acetic acid (IAA) production,⁴⁴ and the *fmo* mutant showed promoted leaf senescence. Caspases have been reported to be associated with programmed cell death in both plants and mammals,⁴⁵ and mutation of *CATHB1* caused delayed leaf senescence. Copper is one of the essential mobile

- (B) Expression patterns of genes in senescence-related modules.
 - (C) Biological GO enrichment of genes in senescence-related modules.
 - (D) Co-expression scores of genes in the two modules that closely correlated with SAG-index or YAG-index.
 - (E) Co-expression networks between selected unreported hub genes and known promoted or delayed SAGs. The selected hub genes and known SAGs are classified according to their functions.
 - (F) Phenotypes of the fourth rosette leaves in mutants of selected hub genes at the indicated ages. The wild-type Col-0, early-senescence mutant *ebf1*, and delayed-senescence mutant *eds16* are used as controls. Representative leaves are shown for each sample. Scale bar, 1 cm.
 - (G) Chlorophyll contents in the leaves shown in (F). Data = mean ± SD, n = 4. The t test statistical significances were indicated with a–g.
 - (H) RT-qPCR analysis of *RBCS1A*, *SAG12*, and *SAG13* expressions in the leaves shown in (F).
- See also Figure S5.

micronutrients that acts as a cofactor in many enzymes and has direct effect on photosynthesis.⁴⁶ We found delayed leaf senescence in a mutant of copper trafficking gene *CCH*, which might be associated with the disruption of copper mobilization from source senescent leaves to sink organs.⁴⁶

Acting as gatekeepers of cell, numerous transporters facilitate the uptake and trafficking of nutrients through diverse mechanisms.⁴⁷ Based on the snRNA-seq data and mutant phenotype estimation, we found the expression of a multidrug and toxic compound extrusion (MATE) transporter *DTX3* (*AT2G04050*) accumulated along leaf development, and mutation of *DTX3* showed delayed leaf senescence (Figures 4F–4H and S5A), supporting the functions of MATE transporters in regulating leaf senescence.⁴⁸ We also found several carbon and nitrogen transporters showed high co-expression scores with SAG index (Figures 4D and 4E), which will be discussed in the next section.

Dynamic leaf-to-sink allocation of carbon and nitrogen

Although leaf-to-sink allocation of carbon and nitrogen plays critical roles in leaf senescence (Figure 4E), a systemic view of how different transporters coordinate the dynamic carbon and nitrogen flows during leaf development has not been achieved.^{49,50} We therefore first examined the cell type- and developmental stage-specific expression patterns of several major carbon and nitrogen transporter families in our rosette datasets (Figures 5A, S5C, and S5D). Then we obtained T-DNA insertion mutants of these carbon and nitrogen transporters and evaluated their dynamic senescence phenotypes (Table S2). We found that the mutants of nine transporters showed altered senescence onset and progression, indicated by leaf color, chlorophyll content changes, and the expression of leaf senescence-associated marker genes (Figures S5E–S5G).

Sugars will eventually be exported transporter (SWEET), sucrose carrier (SUC), and sugar transport protein (STP) are prime transporters mediating sugar efflux from leaf to flower and siliques.⁵¹ We detected *SWEET11*, *SWEET12*, and *SWEET13* being specifically expressed in phloem parenchyma (PP) cells of late senescing stage leaves (Figure 5A), consistent with their phloem loading function.^{28,50–52} We found delayed leaf senescence phenotype in *sweet12* mutant (Figures 5B and S5E–S5G). Although *SWEET11* and *SWEET12* exhibit structural similarities and often function redundantly,⁵¹ the altered phenotype of *sweet12* mutant suggested a unique role of *SWEET12* in leaf senescence regulation. Beside the well-recognized sucrose/H₁ symporter *SUC2*, three other *SUCs* were also detected in the CC of leaf (Figure 5A), among which *SUC4* and *SUC7* were mainly expressed during S5 and S6, respectively.

In contrast to the apoplastic phloem loading route that exports sugars from EPI/MES/PP and imports sugars into CC in late senescing leaves, we found unexpected expression patterns for both exporters and importers, including *SWEET4* and *SWEET5* in CC at early stages, and *STP1*, *STP3*, *STP4*, *STP7*, *STP11*, *STP13*, and *STP14* in non-CC cell types at senescing stages (Figure 5A). These expression patterns implicated putative sugar retrieval routes, which might maximize sugar utility throughout leaf development. Delayed leaf senescence phenotype of *stp3*, *stp4*, *stp7*, *stp13*, and *stp14* mutants implied that the recycle

route might also be involved in leaf senescence regulation (Figures 5B and S5E–S5G; Table S2).

For nitrogen transporters, we confirmed that *UmamiT18* was specifically expressed in the PP cells of late senescing stage leaf (Figure 5A).⁵³ In addition, *UmamiT20*, *UmamiT28*, and *UmamiT29* were also expressed with the same expression pattern (Figure 5A). *UmamiT40* was relatively highly expressed in the late senescing stages of both EPI and MES, while *UmamiT24* was specifically expressed in the late senescing stage of MES (Figure 5A), suggesting direct apoplastic export of amino acids from EPI and MES during leaf senescing stages. The delayed leaf senescence phenotypes of *umamit20*, *umamit29*, and *umamit40* indicated that these three genes are essential for exporting amino acids from mature leaves (Figures 5B and S5E–S5G).

Analogous to the SWEET-SUC transporter pairs involved in sugar allocation, AAAP importers in the CCs mediate amino acid uptake from apoplastic space.⁵⁰ In correspondence, five AAAPs (*AAAP4*, *AAAP10*, *AAAP25*, *AAAP31*, and *AAAP35*) were specifically expressed in CCs of leaves, and four of them were mainly expressed during senescing stages (S4–S6) (Figure 5A). The identification of more CC-specific AAAPs (*AAAP10* and *AAAP31*) than previous single-cell work⁵⁰ reflected the ability of our atlas to estimate chronological coordination between cell-type-specific nitrogen transporters at temporal dimension. We also found several AAAPs highly expressed in EPI (*AAAP20* and *AAAP28*) and MES (*AAAP24* and *AAAP40*) at early leaf expansion stage, implicating their major functions for supplying amino acids to growing leaf cells (Figure 5A).

Besides the main transport forms of nitrogen amino acids in senescing leaves,⁴⁹ nitrate also takes an important role throughout plant development. We found nitrate transporters *NPF6.2* were specifically expressed in the early-stage leaf PP cells (Figure 5A), consistent with its important role in nitrate storage in leaf petiole.⁵⁴ Similar expression patterns were also detected for *NPF1.2*, *NPF2.6*, and *NPF3.1*, indicating potential overlapping roles of these uncharacterized *NPFs* in nitrate storage (Figure 5A). For EPI, MES, and CC, we also detected cell-type-specific *NPFs* during early-stage growth, suggesting the usage of specific nitrate transporters in these cell types for nitrate accumulation (Figure 5A). We noticed that *NRT2.5* showed a senescence-associated increase of expression in all the major cell types in leaf (Figure 5A), consistent with its role in nitrate remobilization.^{30,55}

Because nutrients exported from senescing leaves are mainly used to support the growth of sink organs, we therefore also examined expression patterns of carbon and nitrogen transporters in root, stem, flower, and siliques (Figures 5C, S5C, and S5D). Our results suggested that, in roots, sugars are likely allocated from CCs by SWEET1, SWEET2, and SWEET14 and imported to pericycle cells through SUC2 and SUC4. We also identified *SWEET16* and *SWEET17* being highly expressed in suberized-endodermis cells (Figure 5A), consistent with their function in the vacuolar storage of sugar in roots.⁵⁶ Additionally, *SWEET15* showed similar specific expressions as *SWEET16* and *SWEET17*, indicating potential similar functions. In stem, we detected *SWEET11*, *SWEET12*, and *SWEET13* being specifically expressed in PP cells (Figure 5A), indicating their phloem loading function similar to that in leaf. In flower, sugars might be exported from PP cells by SWEET2, SWEET11, and SWEET12 and then be

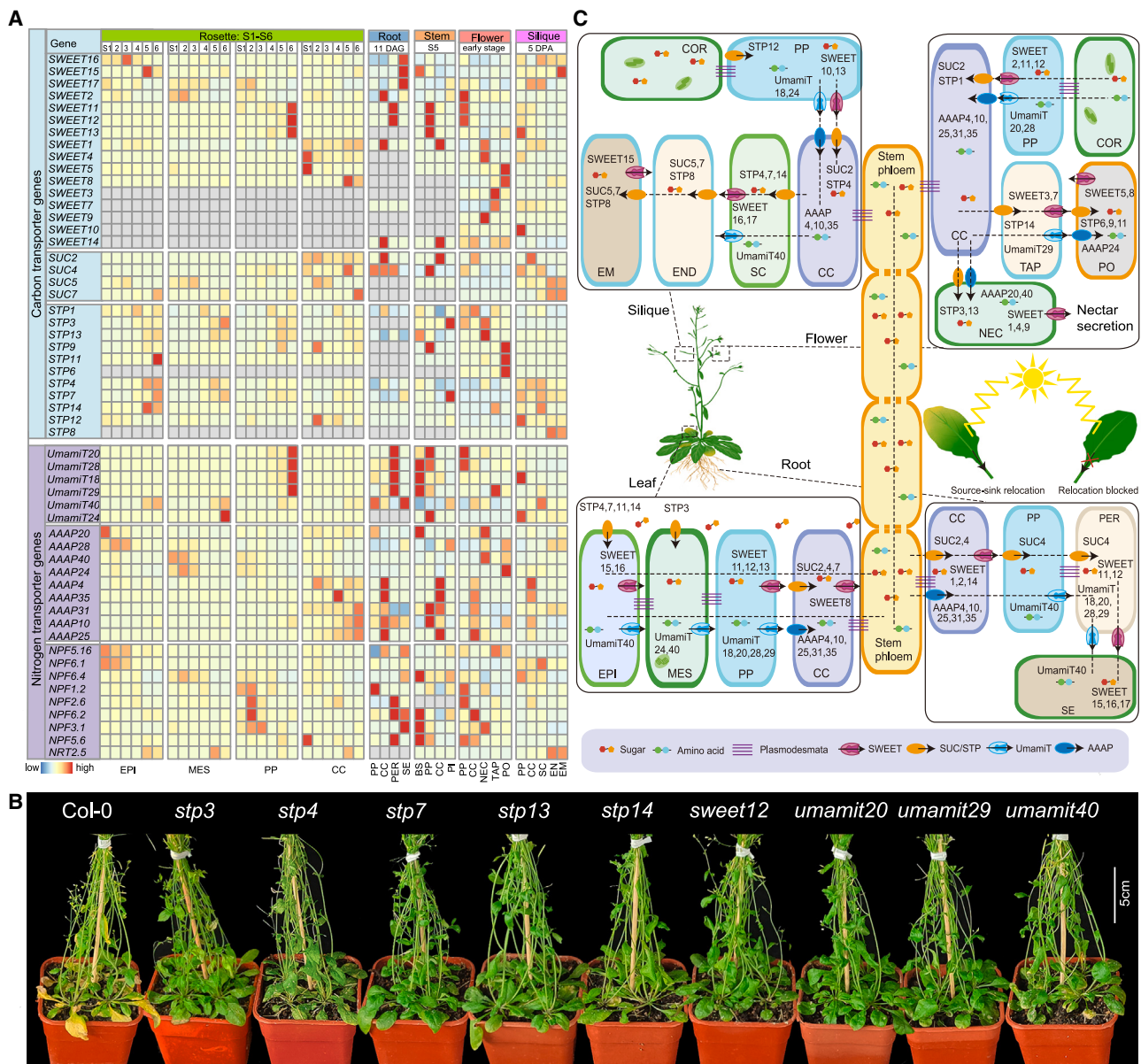


Figure 5. Dynamic source-sink allocation of carbon and nitrogen in leaves and reproductive organs

(A) Cell-type-specific and temporal expression patterns of sugar and nitrogen transporter families in rosette leaves (S1–S6), root (11 days), stem (42 days), developing flower (early stage), and siliques (5 DPA).

(B) Delayed leaf senescence phenotypes of nine sugar and nitrogen transporter mutants at 60 DAG. Scale bars, 5 cm.

(C) A hypothetical working model summarizing the allocation of sugars and amino acids from source senescing leaves to sink flower and siliques. The cell-type-specific transporter compositions are based on transporter genes highly expressed in late senescing leaves (S5–S6), root (11 days), stem (42 days), developing flower (early stage), and siliques (5 DPA).

See also Figure S5. Abbreviations for cell types are provided in Figure 2.

imported to CCs through SUC2 and STP1 (Figures 5A and 5C). In siliques, sugars might be transferred between PP cells and CCs by SWEET10/13–SUC2/STP4 pairs (Figures 5A and 5C), and then the accumulated sugars in siliques were carried to seed coat through STP4, STP7, and STP14 and further exported by SWEET16 and SWEET17 to apoplastic space (Figures 5A and 5C). In addition, we also detected preferentially expressed car-

bon transporters with their roles in specific sink regions of flower and siliques (Figure 5C), such as newly identified SWEET1, SWEET4, and the reported SWEET9⁵⁷ in nectar secretion, SWEET5 and SWEET8 that are known to be involved in pollen development and exine formation,^{58,59} as well as SUC5 in the nutrition allocation of the filial tissues during early seed development.⁶⁰

Similar to carbon transporters, we also detected cell-type-specific compositions of nitrogen transporters in sink organs, root, stem, flower, and siliques (Figures 5A, 5C, S5B, and S5C). A leaf PP-like scenario of *UmamiTs* (*UmamiT18/20/28/29*) was observed in pericycle cell in root and bundle sheath cell in stem (Figure 5A), suggesting pericycle and bundle sheath are key cell types in direct apoplastic export of amino acids. *UmamiT20* and *UmamiT28* mainly expressed in PP cells of flower for potential amino acid unloading, while *UmamiT18* and *UmamiT24* were detected in the same cell type of siliques (Figures 5A and 5C). Moreover, *UmamiT29* was predominantly detected in tapetum cells, suggesting its role for supplying amino acids to the developing pollen cells (Figures 5A and 5C). *UmamiT40* was predominantly detected in seed coat of siliques, implicating its role for delivering amino acids to the interior cell types of developing seeds (Figures 5A and 5C). Interestingly, a leaf CC-like composition of AAAPs (AAAP4/10/25/31/35) was detected in root, stem, flower, and siliques, strengthening the cross-organ conservation of CCs discussed above (Figure 2H). For nitrate transporters, we found specific expression of *NPF3.1* in nectary, *NPF5.16* in tapetum and pollen, and *NRT2.5* in endosperm and embryo, suggesting their specific functions in nitrate accumulation of these sink regions (Figure 5A).

DISCUSSION

Despite the extensive efforts made in clarifying the cellular composition of different plant organs (Table S1), a global single-cell transcriptomic landscape encompassing the dynamic development of various organs is still challenging due to the difficulty in isolating protoplasts from many mature and complex tissues. The snRNA-seq approach has been successfully used in single-cell studies (Table S1) and has demonstrated several advantages in reducing time-consuming digestion, stress-induced transcriptional artifacts, and cell coverage bias.¹⁰ This approach also facilitates the identification of additional cell types that were not detected in previous scRNA-seq studies, such as the mature endodermis cells and trichome cells.^{7,12}

The advantages of the snRNA-seq approach enabled the construction of global cell atlas with multiple organs.⁷⁻⁹ With data available for diverse tissues, it is now possible to perform systematic cross-tissue comparison to resolve cellular heterogeneity across multiple organs. These recently published global cell landscapes and our study all uncovered key TFs regulating conserved cell types across different organs and identified specific regulators associated with cell-specific functions.⁷⁻⁹ Of note, both Lee et al.⁷ and our study explored temporal transcriptional dynamics and coordinated gene expression in multiple major organs of *Arabidopsis*, highlighting the advantage of time-series sampling strategy in single-cell studies that explore plant organ developmental process.

The progressive senescence of leaves is a critical strategy that enables plants to achieve an orderly transition from vegetative to reproductive growth. This process involves both inter- and intra-cell-type heterogeneity during senescence progression, which has been challenging to capture with traditional biochemical and molecular assays. In this study, we formulated

two molecular indexes that provide a unique approach to quantitatively assess the aging state at single-cell resolution. This enables not only the precise characterization of senescence heterogeneity but also the identification of key regulators driving leaf senescence onset and progression. As a proof of concept, we used the dynamics of these two indexes to construct a gene co-expression network and predicted hundreds of promising hub genes that may coordinately regulate the processes of leaf senescence. Future pathway exploration will facilitate the understanding of their functions and regulatory networks on leaf senescence.

Nutrient recycling and exportation are the most important activities of leaves at the final stage of development, but how these processes are spatial-temporally orchestrated among different cell types is largely unclear.^{61,62} Recent single-cell transcriptomic studies have identified several candidate transporters that may coordinate nutrient translocation between multiple cell types in mature leaves.^{28,50} Our study, however, further extended the spectrum of candidate transporters that may compose the chronological changes of nutrient flow from source leaves to sink organs (roots, stem, flowers, and siliques). Beyond the focus on carbon and nitrogen allocation, our atlas also provides a foundational resource for probing other nutrient fluxes, hormone dynamics, and growth regulators across developmental stages.

Limitations of the study

Compared with data generated using protoplasts, snRNA-seq lacks cytoplasmic transcripts, leading to a lower number of genes captured in each cell and posing the challenges for high-resolution cell-type annotation. Nonetheless, cell classification and annotation of this study align with the resolution and confidence standards established by previously published datasets. However, as our primary focus is on leaf senescence and nutrient allocation, which primarily involve well-characterized cell types, this work does not substantially expand the coverage of certain cell types or subcell types compared with previous studies. Moreover, a small fraction of clusters (3.5%, 19 out of 539 clusters) were classified as “unknown” due to the lack of validated marker genes. In the future, annotation of these uncertain clusters will benefit from the growing application of spatial transcriptomics, as well as the ongoing advancements in annotation methodologies. Using the comprehensive single-nucleus atlas as a framework, we found the SAG-index and YAG-index aforementioned could collectively indicate the aging state of single-leaf cells in the model species *Arabidopsis*. Analyses using published bulked mRNA-seq data verified that the SAG-index and YAG-index together could indicate the states of development, differentiation, or stress responses of various *Arabidopsis* organs, as well as leaf development and senescence of *Populus*. However, whether the application of these two indexes could extend to quantify the aging state of other plant species remains to be clarified. Using SAG-index and YAG-index as traits for WGCNA, we identified hundreds of promising hub genes and validated their functions in regulation of leaf senescence. It is now crucial to unravel the gene interactions between our identified hub genes and potential TFs to identify downstream signaling pathways, facilitating the understanding of a full picture of senescence and nutrient allocation from

source to sink. These tasks require substantial research efforts beyond the scope of this study.

RESOURCE AVAILABILITY

Lead contact

Further information and requests for the resources and reagents may be directed to and will be fulfilled by the lead contact, Xun Xu (xuxun@genomics.cn).

Materials availability

All materials used for snRNA-seq and Stereo-seq are commercially available.

Data and code availability

To facilitate further exploration of our single-nucleus *Arabidopsis* atlas, we have deposited the snRNA-seq raw data (<https://db.cngb.org/search/project/CNP0002614/>) and gene metrics (<https://ftp.cngb.org/pub/CNSA/data6/CNP0002614/Other/>) in the CNGB database under accession number CNP0002614. We also developed an online website with detailed description for sampling strategy and cell type annotation (https://db.cngb.org/codeplot/datasets/Arabidopsis_Cell_Atlas). Computer codes used for processing the snRNA-seq analyses are available in GitHub (https://github.com/ctan2020/Arabidopsis_Cell_Atlas).

ACKNOWLEDGMENTS

This work was supported by the Biological Breeding-National Science and Technology Major Project (2023ZD04073 to H. Liu), the National Key Research and Development Program of China (2019YFA0903904 to H.G.), and the Shenzhen Science and Technology Program (KQTD20230301092839007 to C.T.). This work was also supported by the National Natural Science Foundation of China (32230008 to H.G.), the Shenzhen Science and Technology Program (KQTD20190929173906742 to H.G.), and the New Cornerstone Science Foundation (HYPERLINK "gn6:" NCI202235 to H.G.). Parts of the data analysis were supported by the Center for Computational Science and Engineering at the Southern University of Science and Technology. We are grateful to Shu-qiang Chen, Kaimeng Wang, Jing Wang, Yuting Yang, Yunting Huang, Minyue Wang, Xiumei Lin, Zifeng Wang, Shiping Liu, Haixi Sun, Jie Li, Liang Wu, Weiqing Liu, Ning Yang, and Robert J. Schmitz for general technical assistance or discussion.

AUTHOR CONTRIBUTIONS

X.X., H.G., and H. Liu conceived the idea and supervised the work; X. Guo and Yichuan Wang designed the experiments; Y.Z., M.Y., P.X., and Yi Wang collected tissue samples; and X. Guo, C.Z., M.Z., W.S., and H. Lu generated snRNA-seq data. D.Z., Y.Z., and Z.L. estimated the phenotype of mutants. Y.P., Y.Q., and T.P. collected the carbon and nitrogen transporter information and conducted qPCR analysis. C.Z., C.T., W.Y., X. Guo, Yichuan Wang, S.X., D.F., H.Z., and X. Guang performed data analysis. X. Guo, C.Z., C.T., W.Y., L.Y., L.L., H.W., M.Y., P.X., Yi Wang, and M. Liu prepared the figures. C.T., Z.X., and F.W. prepared the website. X.X., H.G., H. Liu, S.K.S., T.W., X.N., H.Y., E.W., and M. Lisby provided relevant advice and reviewed the manuscript. X. Guo, C.Z., Yichuan Wang, C.T., and W.Y. prepared the manuscript with input from all authors. X.X., H.G., and Huan Liu finalized the manuscript. All other authors contributed to the work. All authors read and approved the manuscript for submission.

DECLARATION OF INTERESTS

The authors declare no competing interests.

STAR METHODS

Detailed methods are provided in the online version of this paper and include the following:

KEY RESOURCES TABLE

EXPERIMENTAL MODEL AND STUDY PARTICIPANT DETAILS

- Plant material and growth condition

METHOD DETAILS

- Plant materials preparation
- Single nucleus isolation
- Single-nucleus transcriptome sequencing (snRNA-seq) and data processing
- Quality control and unsupervised clustering
- Identification of cluster-specific differentially expressed genes
- Cell type annotation
- Correlation estimation between different cell types or tissues
- Spatial transcriptomes generated by Stereo-seq
- Spatial transcriptomic analyses
- Gene Ontology term enrichment analysis
- Pseudotime analysis
- Organ- and cell-type-enriched transcription factors analysis
- Leaf SAG-index and YAG-index modeling and application in bulked RNA-seq data
- Weighted gene coexpression network analysis (WGCNA)
- Marker line generation and confocal observation
- Age-dependent leaf senescence assays
- RNA extraction and quantitative real-time PCR analysis

QUANTIFICATION AND STATISTICAL ANALYSIS

SUPPLEMENTAL INFORMATION

Supplemental information can be found online at <https://doi.org/10.1016/j.cell.2025.03.024>.

Received: October 15, 2023

Revised: July 30, 2024

Accepted: March 12, 2025

Published: April 11, 2025

REFERENCES

1. Guo, Y., Ren, G., Zhang, K., Li, Z., Miao, Y., and Guo, H. (2021). Leaf senescence: progression, regulation, and application. Mol. Hortic. 1, 5. <https://doi.org/10.1186/s43897-021-00006-9>.
2. Yin, R., Chen, R., Xia, K., and Xu, X. (2024). A single-cell transcriptome atlas reveals the trajectory of early cell fate transition during callus induction in *Arabidopsis*. Plant Commun. 5, 100941. <https://doi.org/10.1016/j.xpc.2024.100941>.
3. Liew, L.C., You, Y., Auroux, L., Oliva, M., Peirats-Llobet, M., Ng, S., Tamiru-Oli, M., Berkowitz, O., Hong, U.V.T., Haslem, A., et al. (2024). Establishment of single-cell transcriptional states during seed germination. Nat. Plants 10, 1418–1434. <https://doi.org/10.1038/s41477-024-01771-3>.
4. Han, X., Zhang, Y., Lou, Z., Li, J., Wang, Z., Gao, C., Liu, Y., Ren, Z., Liu, W., Li, B., et al. (2023). Time series single-cell transcriptional atlases reveal cell fate differentiation driven by light in *Arabidopsis* seedlings. Nat. Plants 9, 2095–2109. <https://doi.org/10.1038/s41477-023-01544-4>.
5. Qin, Y., Sun, M., Li, W., Xu, M., Shao, L., Liu, Y., Zhao, G., Liu, Z., Xu, Z., You, J., et al. (2022). Single-cell RNA-seq reveals fate determination control of an individual fibre cell initiation in cotton (*Gossypium hirsutum*). Plant Biotechnol. J. 20, 2372–2388. <https://doi.org/10.1111/pbi.13918>.
6. Bai, Y., Liu, H., Lyu, H., Su, L., Xiong, J., and Cheng, Z.M.M. (2022). Development of a single-cell atlas for woodland strawberry (*Fragaria vesca*) leaves during early *Botrytis cinerea* infection using single-cell RNA-seq. Hortic. Res. 9, uhab055. <https://doi.org/10.1093/hr/uhab055>.
7. Lee, T.A., Nobori, T., Illouz-Eliaz, N., Xu, J., Jow, B., Nery, J.R., and Ecker, J.R. (2023). A single-nucleus atlas of seed-to-seed development in *Arabidopsis*. Preprint at bioRxiv. <https://doi.org/10.1101/2023.03.23.533992>.
8. Zhang, X., Luo, Z., Marand, A.P., Yan, H., Jang, H., Bang, S., Mendieta, J.P., Minow, M.A.A., and Schmitz, R.J. (2025). A spatially resolved

- multiomic single-cell atlas of soybean development. *Cell* 188, 550–567.e19. <https://doi.org/10.1016/j.cell.2024.10.050>.
9. Cervantes-Perez, S.A., Thibivilliers, S., Amini, S., Pelletier, J.M., Meyer, I., Xu, H., Tenant, S., Ma, P., Sprueill, C.M., Farmer, A.D., et al. (2024). Tabula Glycine: The whole-soybean single-cell resolution transcriptome atlas. Preprint at bioRxiv. <https://doi.org/10.1101/2024.07.08.602332>.
10. Wang, K., Zhao, C., Xiang, S., Duan, K., Chen, X., Guo, X., and Sahu, S.K. (2023). An optimized FACS-free single-nucleus RNA sequencing (snRNA-seq) method for plant science research. *Plant Sci.* 326, 111535. <https://doi.org/10.1016/j.plantsci.2022.111535>.
11. Han, L., Wei, X., Liu, C., Volpe, G., Zhuang, Z., Zou, X., Wang, Z., Pan, T., Yuan, Y., Zhang, X., et al. (2022). Cell transcriptomic atlas of the non-human primate *Macaca fascicularis*. *Nature* 604, 723–731. <https://doi.org/10.1038/s41586-022-04587-3>.
12. Farmer, A., Thibivilliers, S., Ryu, K.H., Schiefelbein, J., and Libault, M. (2021). Single-nucleus RNA and ATAC sequencing reveals the impact of chromatin accessibility on gene expression in *Arabidopsis* roots at the single-cell level. *Mol. Plant* 14, 372–383. <https://doi.org/10.1016/j.molp.2021.01.001>.
13. Wendrich, J.R., Yang, B., Vandamme, N., Verstaen, K., Smet, W., Van de Velde, C., Minne, M., Wybouw, B., Mor, E., Arents, H.E., et al. (2020). Vascular transcription factors guide plant epidermal responses to limiting phosphate conditions. *Science* 370, eaay4970. <https://doi.org/10.1126/science.aay4970>.
14. Ryu, K.H., Huang, L., Kang, H.M., and Schiefelbein, J. (2019). Single-cell RNA sequencing resolves molecular relationships among individual plant cells. *Plant Physiol.* 179, 1444–1456. <https://doi.org/10.1104/pp.18.01482>.
15. Jean-Baptiste, K., McFaline-Figueroa, J.L., Alexandre, C.M., Dorritt, M.W., Saunders, L., Bubb, K.L., Trapnell, C., Fields, S., Queitsch, C., and Cuperus, J.T. (2019). Dynamics of gene expression in single root cells of *Arabidopsis thaliana*. *Plant Cell* 31, 993–1011. <https://doi.org/10.1105/tpc.18.00785>.
16. Shahani, R., Hsu, C.W., Nolan, T.M., Cole, B.J., Taylor, I.W., Greenstreet, L., Zhang, S., Afanassiev, A., Vlot, A.H.C., Schiebinger, G., et al. (2022). A single-cell *Arabidopsis* root atlas reveals developmental trajectories in wild-type and cell identity mutants. *Dev. Cell* 57, 543–560.e9. <https://doi.org/10.1016/j.devcel.2022.01.008>.
17. Speck, T., and Burgert, I. (2011). Plant stems: functional design and mechanics. *Annu. Rev. Mater. Res.* 41, 169–193. <https://doi.org/10.1146/annurev-matsci-062910-100425>.
18. Chen, A., Liao, S., Cheng, M., Ma, K., Wu, L., Lai, Y., Qiu, X., Yang, J., Xu, J., Hao, S., et al. (2022). Spatiotemporal transcriptomic atlas of mouse organogenesis using DNA nanoball-patterned arrays. *Cell* 185, 1777–1792.e21. <https://doi.org/10.1016/j.cell.2022.04.003>.
19. Cai, S., and Lashbrook, C.C. (2008). Stamen abscission zone transcriptome profiling reveals new candidates for abscission control: enhanced retention of floral organs in transgenic plants overexpressing *Arabidopsis* ZINC FINGER PROTEIN2. *Plant Physiol.* 146, 1305–1321. <https://doi.org/10.1104/pp.107.110908>.
20. Misra, C.S., Sousa, A.G.G., Barros, P.M., Kermanov, A., and Becker, J.D. (2023). Cell-type-specific alternative splicing in the *Arabidopsis* germline. *Plant Physiol.* 192, 85–101. <https://doi.org/10.1093/plphys/kiac574>.
21. Petricka, J.J., Winter, C.M., and Benfey, P.N. (2012). Control of *Arabidopsis* root development. *Annu. Rev. Plant Biol.* 63, 563–590. <https://doi.org/10.1146/annurev-plant-042811-105501>.
22. Zhong, R., Lee, C., and Ye, Z.H. (2010). Global analysis of direct targets of secondary wall NAC master switches in *Arabidopsis*. *Mol. Plant* 3, 1087–1103. <https://doi.org/10.1093/mp/ssq062>.
23. Zhu, Y., and Li, L. (2021). Multi-layered regulation of plant cell wall thickening. *Plant Cell Physiol.* 62, 1867–1873. <https://doi.org/10.1093/pcp/pcab152>.
24. Thirugnanasambantham, K., Durairaj, S., Saravanan, S., Karikalan, K., Muralidaran, S., and Islam, V.I.H. (2015). Role of ethylene response transcription factor (ERF) and its regulation in response to stress encountered by plants. *Plant Mol. Biol. Rep.* 33, 347–357. <https://doi.org/10.1007/s11105-014-0799-9>.
25. Johnson, C.S., Kolevski, B., and Smyth, D.R. (2002). *TRANSPARENT TESTA GLABRA2*, a trichome and seed coat development gene of *Arabidopsis*, encodes a WRKY transcription factor. *Plant Cell* 14, 1359–1375. <https://doi.org/10.1105/tpc.001404>.
26. Piya, S., Liu, J., Burch-Smith, T., Baum, T.J., and Hewezi, T. (2020). A role for *Arabidopsis* growth-regulating factors 1 and 3 in growth-stress antagonism. *J. Exp. Bot.* 71, 1402–1417. <https://doi.org/10.1093/jxb/erz502>.
27. Hagelthorn, L., Monfared, M.M., Talo, A., Harmon, F.G., and Fletcher, J.C. (2023). Unique and overlapping functions for the transcriptional regulators KANADI1 and ULTRAPETALA1 in *Arabidopsis* gynoecium and stamen gene regulation. *Plant Direct* 7, e496. <https://doi.org/10.1002/pld3.496>.
28. Kim, J.Y., Symeonidi, E., Pang, T.Y., Denyer, T., Weidauer, D., Bezrutczyk, M., Miras, M., Zöllner, N., Hartwig, T., Wudick, M.M., et al. (2021). Distinct identities of leaf phloem cells revealed by single cell transcriptomics. *Plant Cell* 33, 511–530. <https://doi.org/10.1093/plcell/koaa060>.
29. Andriankaja, M., Dhondt, S., De Bodt, S., Vanhaeren, H., Coppens, F., De Milde, L., Mühlensbock, P., Skirycz, A., Gonzalez, N., Beemster, G.T.S., et al. (2012). Exit from proliferation during leaf development in *Arabidopsis thaliana*: a not-so-gradual process. *Dev. Cell* 22, 64–78. <https://doi.org/10.1016/j.devcel.2011.11.011>.
30. Breeze, E., Harrison, E., McHattie, S., Hughes, L., Hickman, R., Hill, C., Kiddle, S., Kim, Y.S., Penfold, C.A., Jenkins, D., et al. (2011). High-resolution temporal profiling of transcripts during *Arabidopsis* leaf senescence reveals a distinct chronology of processes and regulation. *Plant Cell* 23, 873–894. <https://doi.org/10.1105/tpc.111.083345>.
31. Li, Z., Zhang, Y., Zou, D., Zhao, Y., Wang, H.L., Zhang, Y., Xia, X., Luo, J., Guo, H., and Zhang, Z. (2020). LSD 3.0: a comprehensive resource for the leaf senescence research community. *Nucleic Acids Res.* 48, D1069–D1075. <https://doi.org/10.1093/nar/gkz898>.
32. Procko, C., Lee, T., Borsuk, A., Bargmann, B.O.R., Dabi, T., Nery, J.R., Estelle, M., Baird, L., O'Connor, C., Brodersen, C., et al. (2022). Leaf cell-specific and single-cell transcriptional profiling reveals a role for the palisade layer in UV light protection. *Plant Cell* 34, 3261–3279. <https://doi.org/10.1093/plcell/koac167>.
33. Woo, H.R., Kim, H.J., Lim, P.O., and Nam, H.G. (2019). Leaf Senescence: systems and dynamics aspects. *Annu. Rev. Plant Biol.* 70, 347–376. <https://doi.org/10.1146/annurev-aplant-050718-095859>.
34. Le Gloanec, C.L., Gómez-Felipe, A., Alimchandani, V., Branchini, E., Bauer, A., Routier-Kierzkowska, A.L., and Kierzkowski, D. (2024). Modulation of cell differentiation and growth underlies the shift from bud protection to light capture in cauline leaves. *Plant Physiol.* 196, 1214–1230. <https://doi.org/10.1093/plphys/kiae408>.
35. Barros, J.A.S., Magen, S., Lapidot-Cohen, T., Rosental, L., Brotman, Y., Araújo, W.L., and Avin-Wittenberg, T. (2021). Autophagy is required for lipid homeostasis during dark-induced senescence. *Plant Physiol.* 185, 1542–1558. <https://doi.org/10.1093/plphys/kiaa120>.
36. Kim, H.J., Hong, S.H., Kim, Y.W., Lee, I.H., Jun, J.H., Phee, B.K., Rupak, T., Jeong, H., Lee, Y., Hong, B.S., et al. (2014). Gene regulatory cascade of senescence-associated NAC transcription factors activated by ETHYLENE-INSENSITIVE2-mediated leaf senescence signalling in *Arabidopsis*. *J. Exp. Bot.* 65, 4023–4036. <https://doi.org/10.1093/jxb/eru112>.
37. Potuschak, T., Lechner, E., Parmentier, Y., Yanagisawa, S., Grava, S., Koncz, C., and Genschik, P. (2003). EIN3-dependent regulation of plant ethylene hormone signaling by two *Arabidopsis* F box proteins: EBF1 and EBF2. *Cell* 115, 679–689. [https://doi.org/10.1016/s0092-8674\(03\)00968-1](https://doi.org/10.1016/s0092-8674(03)00968-1).
38. Morris, K., Mackerness, S.A.H., Page, T., John, C.F., Murphy, A.M., Carr, J.P., and Buchanan-Wollaston, V. (2000). Salicylic acid has a role in regulating gene expression during leaf senescence. *Plant J.* 23, 677–685. <https://doi.org/10.1046/j.1365-313x.2000.00836.x>.

39. James, M., Poret, M., Masclaux-Daubresse, C., Marmagne, A., Coquet, L., Jouenne, T., Chan, P., Trouverie, J., and Etienne, P. (2018). SAG12, a major cysteine protease involved in nitrogen allocation during senescence for seed production in *Arabidopsis thaliana*. *Plant Cell Physiol.* 59, 2052–2063. <https://doi.org/10.1093/pcp/pcy125>.
40. Izumi, M., Tsunoda, H., Suzuki, Y., Makino, A., and Ishida, H. (2012). *RBCS1A* and *RBCS3B*, two major members within the *Arabidopsis RBCS* multigene family, function to yield sufficient Rubisco content for leaf photosynthetic capacity. *J. Exp. Bot.* 63, 2159–2170. <https://doi.org/10.1093/jxb/err434>.
41. Ritte, G., Lloyd, J.R., Eckermann, N., Rottmann, A., Kossmann, J., and Steup, M. (2002). The starch-related R1 protein is an α -glucan, water dikinase. *Proc. Natl. Acad. Sci. USA* 99, 7166–7171. <https://doi.org/10.1073/pnas.062053099>.
42. Heintz, C., Doktor, T.K., Lanjuin, A., Escoubas, C.C., Zhang, Y., Weir, H.J., Dutta, S., Silva-García, C.G., Bruun, G.H., Morantte, I., et al. (2017). Splicing factor 1 modulates dietary restriction and TORC1 pathway longevity in *C. elegans*. *Nature* 541, 102–106. <https://doi.org/10.1038/nature20789>.
43. Wang, H.L., Zhang, Y., Wang, T., Yang, Q., Yang, Y., Li, Z., Li, B., Wen, X., Li, W., Yin, W., et al. (2021). An alternative splicing variant of PtRD26 delays leaf senescence by regulating multiple NAC transcription factors in *Populus*. *Plant Cell* 33, 1594–1614. <https://doi.org/10.1093/plcell/koab046>.
44. Cao, X., Yang, H., Shang, C., Ma, S., Liu, L., and Cheng, J. (2019). The roles of auxin biosynthesis YUCCA gene family in plants. *Int. J. Mol. Sci.* 20, 6343. <https://doi.org/10.3390/ijms20246343>.
45. Ge, Y., Cai, Y.M., Bonneau, L., Rotari, V., Danon, A., McKenzie, E.A., McLellan, H., Mach, L., and Gallois, P. (2016). Inhibition of cathepsin B by caspase-3 inhibitors blocks programmed cell death in *Arabidopsis*. *Cell Death Differ.* 23, 1493–1501. <https://doi.org/10.1038/cdd.2016.34>.
46. Mir, A.R., Pichtel, J., and Hayat, S. (2021). Copper: uptake, toxicity and tolerance in plants and management of Cu-contaminated soil. *Biometals* 34, 737–759. <https://doi.org/10.1007/s10534-021-00306-z>.
47. Himmelblau, E., and Amasino, R.M. (2001). Nutrients mobilized from leaves of *Arabidopsis thaliana* during leaf senescence. *J. Plant Physiol.* 158, 1317–1323. <https://doi.org/10.1078/0176-1617-00608>.
48. Upadhyay, N., Kar, D., Deepak Mahajan, B., Nanda, S., Rahiman, R., Panchakshari, N., Bhagavatula, L., and Datta, S. (2019). The multitasking abilities of MATE transporters in plants. *J. Exp. Bot.* 70, 4643–4656. <https://doi.org/10.1093/jxb/erz246>.
49. Tegeder, M., and Masclaux-Daubresse, C. (2018). Source and sink mechanisms of nitrogen transport and use. *New Phytol.* 217, 35–53. <https://doi.org/10.1111/nph.14876>.
50. Kim, J.Y., Loo, E.P.I., Pang, T.Y., Lercher, M., Frommer, W.B., and Wudick, M.M. (2021). Cellular export of sugars and amino acids: role in feeding other cells and organisms. *Plant Physiol.* 187, 1893–1914. <https://doi.org/10.1093/plphys/kiab228>.
51. Chen, L.Q., Qu, X.Q., Hou, B.H., Sosso, D., Osorio, S., Fernie, A.R., and Frommer, W.B. (2012). Sucrose efflux mediated by SWEET proteins as a key step for phloem transport. *Science* 335, 207–211. <https://doi.org/10.1126/science.1213351>.
52. Cayla, T., Le Hir, R., and Dinant, S. (2019). Live-cell imaging of fluorescently tagged phloem proteins with confocal microscopy. *Methods Mol. Biol.* 2014, 95–108. https://doi.org/10.1007/978-1-4939-9562-2_8.
53. Ladwig, F., Stahl, M., Ludewig, U., Hirner, A.A., Hammes, U.Z., Stadler, R., Harter, K., and Koch, W. (2012). Siliques are Red1 from *Arabidopsis* acts as a bidirectional amino acid transporter that is crucial for the amino acid homeostasis of siliques. *Plant Physiol.* 158, 1643–1655. <https://doi.org/10.1104/pp.111.192583>.
54. Chiu, C.C., Lin, C.S., Hsia, A.P., Su, R.C., Lin, H.L., and Tsay, Y.F. (2004). Mutation of a nitrate transporter, AtNRT1: 4, results in a reduced petiole nitrate content and altered leaf development. *Plant Cell Physiol.* 45, 1139–1148. <https://doi.org/10.1093/pcp/pch143>.
55. Lezhneva, L., Kiba, T., Feria-Bourrelier, A.B., Lafouge, F., Boutet-Mercey, S., Zoufan, P., Sakakibara, H., Daniel-Vedele, F., and Krapp, A. (2014). The *Arabidopsis* nitrate transporter NRT 2.5 plays a role in nitrate acquisition and remobilization in nitrogen-starved plants. *Plant J.* 80, 230–241. <https://doi.org/10.1111/tpj.12626>.
56. Guo, W.J., Nagy, R., Chen, H.Y., Pfrunder, S., Yu, Y.C., Santelia, D., Frommer, W.B., and Martinola, E. (2014). SWEET17, a facilitative transporter, mediates fructose transport across the tonoplast of *Arabidopsis* roots and leaves. *Plant Physiol.* 164, 777–789. <https://doi.org/10.1104/pp.113.232751>.
57. Lin, I.W., Sosso, D., Chen, L.Q., Gase, K., Kim, S.G., Kessler, D., Klinkenberg, P.M., Gorder, M.K., Hou, B.H., Qu, X.Q., et al. (2014). Nectar secretion requires sucrose phosphate synthases and the sugar transporter SWEET9. *Nature* 508, 546–549. <https://doi.org/10.1038/nature13082>.
58. Chen, L.Q., Hou, B.H., Lalonde, S., Takanaga, H., Hartung, M.L., Qu, X.Q., Guo, W.J., Kim, J.G., Underwood, W., Chaudhuri, B., et al. (2010). Sugar transporters for intercellular exchange and nutrition of pathogens. *Nature* 468, 527–532. <https://doi.org/10.1038/nature09606>.
59. Sun, M.X., Huang, X.Y., Yang, J., Guan, Y.F., and Yang, Z.N. (2013). *Arabidopsis* RPG1 is important for primexine deposition and functions redundantly with RPG2 for plant fertility at the late reproductive stage. *Plant Reprod.* 26, 83–91. <https://doi.org/10.1007/s00497-012-0208-1>.
60. Baud, S., Wuillème, S., Lemoine, R., Kronenberger, J., Caboche, M., Lepiniec, L., and Rochat, C. (2005). The AtSUC5 sucrose transporter specifically expressed in the endosperm is involved in early seed development in *Arabidopsis*. *Plant J.* 43, 824–836. <https://doi.org/10.1111/j.1365-313X.2005.02496.x>.
61. Kanoja, A., Shrestha, D.K., and Dijkwel, P.P. (2021). Primary metabolic processes as drivers of leaf ageing. *Cell. Mol. Life Sci.* 78, 6351–6364. <https://doi.org/10.1007/s00018-021-03896-6>.
62. Kim, J. (2019). Sugar metabolism as input signals and fuel for leaf senescence. *Genes Genomics* 41, 737–746. <https://doi.org/10.1007/s13258-019-00804-y>.
63. Shi, Q., Liu, S., Kristiansen, K., and Liu, L. (2022). The FASTQ+ format and PISA. *Bioinformatics* 38, 4639–4642. <https://doi.org/10.1093/bioinformatics/btac562>.
64. Dobin, A., Davis, C.A., Schlesinger, F., Drenkow, J., Zaleski, C., Jha, S., Batut, P., Chaisson, M., and Gingeras, T.R. (2013). STAR: ultrafast universal RNA-seq aligner. *Bioinformatics* 29, 15–21. <https://doi.org/10.1093/bioinformatics/bts635>.
65. Young, M.D., and Behjati, S. (2020). SoupX removes ambient RNA contamination from droplet-based single-cell RNA sequencing data. *GigaScience* 9, gaa151. <https://doi.org/10.1093/gigascience/gaa151>.
66. Stuart, T., Butler, A., Hoffman, P., Hafemeister, C., Papalexi, E., Mauck, W. M., 3rd, Hao, Y., Stoeckius, M., Smibert, P., and Satija, R. (2019). Comprehensive Integration of Single-Cell Data. *Cell* 177, 1888–1902.e21. <https://doi.org/10.1016/j.cell.2019.05.031>
67. McGinnis, C.S., Murrow, L.M., and Gartner, Z.J. (2019). DoubletFinder: doublet detection in single-cell RNA sequencing data using artificial nearest neighbors. *Cell Syst.* 8, 329–337.e4. <https://doi.org/10.1016/j.cels.2019.03.003>.
68. Korsunsky, I., Millard, N., Fan, J., Slowikowski, K., Zhang, F., Wei, K., Baglaenko, Y., Brenner, M., Loh, P.R., and Raychaudhuri, S. (2019). Fast, sensitive and accurate integration of single-cell data with Harmony. *Nat. Methods* 16, 1289–1296. <https://doi.org/10.1038/s41592-019-0619-0>.
69. Wu, T., Hu, E., Xu, S., Chen, M., Guo, P., Dai, Z., Feng, T., Zhou, L., Tang, W., Zhan, L., et al. (2021). clusterProfiler 4.0: A universal enrichment tool for interpreting omics data. *Innovation* 2, 100141. <https://doi.org/10.1016/j.xinn.2021.100141>.
70. Yu, G., Wang, L.G., Yan, G.R., and He, Q.Y. (2015). DOSE: an R/Bioconductor package for Disease Ontology Semantic and Enrichment analysis. *Bioinformatics* 31, 608–609. <https://doi.org/10.1093/bioinformatics/btu684>.

71. Trapnell, C., Cacchiarelli, D., Grimsby, J., Pokharel, P., Li, S., Morse, M., Lennon, N.J., Livak, K.J., Mikkelsen, T.S., Rinn, J.L., et al. (2014). The dynamics and regulators of cell fate decisions are revealed by pseudotemporal ordering of single cells. *Nat. Biotechnol.* 32, 381–386. <https://doi.org/10.1038/nbt.2859>.
72. Cao, J., Spielmann, M., Qiu, X., Huang, X., Ibrahim, D.M., Hill, A.J., Zhang, F., Mundlos, S., Christiansen, L., Steemers, F.J., et al. (2019). The single-cell transcriptional landscape of mammalian organogenesis. *Nature* 566, 496–502. <https://doi.org/10.1038/s41586-019-0969-x>.
73. Zhang, Y., Park, C., Bennett, C., Thornton, M., and Kim, D. (2021). Rapid and accurate alignment of nucleotide conversion sequencing reads with HISAT-3N. *Genome Res.* 31, 1290–1295. <https://doi.org/10.1101/gr.275193.120>.
74. Pertea, M., Kim, D., Pertea, G.M., Leek, J.T., and Salzberg, S.L. (2016). Transcript-level expression analysis of RNA-seq experiments with HISAT, StringTie and Ballgown. *Nat. Protoc.* 11, 1650–1667. <https://doi.org/10.1038/nprot.2016.095>.
75. Shumate, A., Wong, B., Pertea, G., and Pertea, M. (2022). Improved transcriptome assembly using a hybrid of long and short reads with StringTie. *PLoS Comput. Biol.* 18, e1009730. <https://doi.org/10.1371/journal.pcbi.1009730>.
76. Langfelder, P., and Horvath, S. (2008). WGCNA: an R package for weighted correlation network analysis. *BMC Bioinf.* 9, 1–13. <https://doi.org/10.1186/1471-2105-9-559>.
77. Shannon, P., Markiel, A., Ozier, O., Baliga, N.S., Wang, J.T., Ramage, D., Amin, N., Schwikowski, B., and Ideker, T. (2003). Cytoscape: a software environment for integrated models of biomolecular interaction networks. *Genome Res.* 13, 2498–2504. <https://doi.org/10.1101/gr.123930>.
78. R Core Team (2021). R: A Language and Environment for Statistical Computing (Version 4.1.2) (Vienna, Austria: R Foundation for Statistical Computing). <https://www.R-project.org/>.
79. Chang, Y.M., Lin, H.H., Liu, W.Y., Yu, C.P., Chen, H.J., Wartini, P.P., Kao, Y.Y., Wu, Y.H., Lin, J.J., Lu, M. Y.J., et al. (2019). Comparative transcriptomics method to infer gene coexpression networks and its applications to maize and rice leaf transcriptomes. *Proc. Natl. Acad. Sci. USA* 116, 3091–3099. <https://doi.org/10.1073/pnas.1817621116>.
80. Lu, H., Gordon, M.I., Amarasinghe, V., and Strauss, S.H. (2020). Extensive transcriptome changes during seasonal leaf senescence in field-grown black cottonwood (*Populus trichocarpa* *Nisqually-1*). *Sci. Rep.* 10, 6581. <https://doi.org/10.1038/s41598-020-63372-2>.
81. Li, P., He, Y., Xiao, L., Quan, M., Gu, M., Jin, Z., Zhou, J., Li, L., Bo, W., Qi, W., et al. (2024). Temporal dynamics of genetic architecture governing leaf development in *Populus*. *New Phytol.* 242, 1113–1130. <https://doi.org/10.1111/nph.19649>.
82. Huang, L., Wen, X., Jin, L., Han, H., and Guo, H. (2024). HOOKLESS1 acetylates AUTOPHAGY-RELATED PROTEIN18a to promote autophagy during nutrient starvation in *Arabidopsis*. *Plant Cell* 36, 136–157. <https://doi.org/10.1093/plcell/koad252>.
83. Zhang, Y., Gao, Y., Wang, H.L., Kan, C., Li, Z., Yang, X., Yin, W., Xia, X., Nam, H.G., Li, Z., et al. (2021). *Verticillium dahliae* secretory effector PevD1 induces leaf senescence by promoting ORE1-mediated ethylene biosynthesis. *Mol. Plant* 14, 1901–1917. <https://doi.org/10.1016/j.molp.2021.07.014>.
84. Kim, H.J., Park, J.H., Kim, J., Kim, J.J., Hong, S., Kim, J., Kim, J.H., Woo, H.R., Hyeon, C., Lim, P.O., et al. (2018). Time-evolving genetic networks reveal a NAC troika that negatively regulates leaf senescence in *Arabidopsis*. *Proc. Natl. Acad. Sci. USA* 115, e4930–e4939. <https://doi.org/10.1073/pnas.1721523115>.
85. Schmittgen, T.D., and Livak, K.J. (2008). Analyzing real-time PCR data by the comparative CT method. *Nat. Protoc.* 3, 1101–1108. <https://doi.org/10.1038/nprot.2008.73>.

STAR★METHODS

KEY RESOURCES TABLE

REAGENT or RESOURCE	SOURCE	IDENTIFIER
Biological samples		
<i>Arabidopsis thaliana</i> ; Columbia-0 (Col-0)	This study	N/A
<i>Arabidopsis thaliana</i> mutants	AraShare	https://www.arashare.cn/index/
Chemicals, peptides, and recombinant proteins		
Sucrose	Sangon Biotsch	A502792-0500
MgCl ₂	Beyotime	ST269
1M Tris-HCl	Beyotime	ST788-500ml
0.1 M DTT	BGI	01B022BM
RNase inhibitor	BGI	LS-EZ-E-00006P
PMSF (100mM)	Beyotime	ST506
40µm Cell Strainer	WHB SCIENTIFIC	WHB-40µm
CellTrics® 30 µm, sterile	SYSMEX PARTEC	04-004-2326
Triton X-100	SIGMA	T8787-50ML
Percoll	Solarbio	P8370-100ml
BSA	Aladdin	A116563-25g
1×PBS Buffer	Sangon Biotsch	B540626-0500
DAPI	Beyotime	C1005
DNBelab C Series Single-Cell Library Prep Set	MGI	1000021082
Qubit ssDNA Assay Kit	Invitrogen	Q10212
Nuclease-free water	Ambion	AM9937
OCT	SAKURA	4583
HCl	DongJiang	N/A
Methanol	Sigma-Aldrich	179337-500ML
Exonuclease I	NEB	M0293L
Ethonal	XILONG SCIENTIFIC	12803405
RNA kits	TransGen Biotech	ER301
cDNA synthesis kit	TransGen Biotech	AT341
RT-qPCR kit	Welab Biotech	W812014
Deposited data		
snRNA-seq data	This study	CNGB: https://db.cngb.org/codeplot/datasets/Arabidopsis_Cell_Atlas
All gene metrics	This study	CNGB: https://db.cngb.org/codeplot/datasets/Arabidopsis_Cell_Atlas
Computer codes	This study	https://github.com/cтан2020/Arabidopsis_Cell_Atlas
Molecular cloning primers		
pQG110- RPGE2FLGFLPLP:5'-CAAGCTTG CATGCCTGCAGCCATTGCGATTATTGATC-3'	This study	N/A
pQG110- RPGE2FL-GFP-RP:5'-CCTTGCTC ACCATGTCGACGTCGTCGGATTCTTAGATG-3'	This study	N/A
RT-qPCR primers		
qUBC21F:5'-TCAAATGGACCGCTTTATC-3'	This study	N/A
qUBC21R:5'-CACAGACTGAAGCGTCCAAG-3'	This study	N/A
qSAG12F:5'-CAGCTGCGGATGTTGTTG-3'	This study	N/A
qSAG12R:5'-CCACTTCTCCCCATTTG-3'	This study	N/A

(Continued on next page)

Continued

REAGENT or RESOURCE	SOURCE	IDENTIFIER
qSAG13F:5'-CTTCCACTCCTAACACTTG-3'	This study	N/A
qSAG13R:5'-GACAACATAAGGACGAACCTTG-3'	This study	N/A
qRBCS1AF:5'-AAGTTGACTACCTTATCCGCAA-3'	This study	N/A
qRBCS1AR:5'-CTTCCACTCCTAACACTTG-3'	This study	N/A
Software and algorithms		
PISA v1.1.0	Shi et al. ⁶³	https://github.com/shiquan/PISA
STAR v2.7.4a	Dobin et al. ⁶⁴	https://github.com/alexdobin/STAR/releases/tag/2.7.4a
SoupX v1.4.8	Young and Behjati ⁶⁵	https://mirrors.aliyun.com/CRAN/src/contrib/Archive/SoupX/
Seurat v3.2.1	Stuart et al. ⁶⁶	https://github.com/satijalab/seurat/releases/tag/v3.2.1
DoubletFinder	McGinnis et al. ⁶⁷	https://github.com/chris-mcginnis-ucsf/DoubletFinder
Harmony	Korsunsky et al. ⁶⁸	https://github.com/immunogenomics/harmony
clusterProfiler v4.0	Wu et al. ⁶⁹	https://github.com/GuangchuangYu/enrichment4GTEx_clusterProfiler
DOSE	Yu et al. ⁷⁰	https://github.com/YuLab-SMU/DOSE
Monocle2 v2.18.0	Trapnell et al. ⁷¹	https://github.com/MaxMeieran/monocle2
Monocle3 v1.0.0	Cao et al. ⁷²	https://github.com/cole-trapnell-lab/monocle3/releases
HISAT2 v2.2.1	Zhang et al. ^{73,74}	https://daehwankimlab.github.io/hisat2/
StringTie v1.3.6	Shumate et al., 2022 ⁷⁵	https://github.com/gpertea/stringtie
WGCNA v1.68	Langfelder and Horvath ⁷⁶	https://cran.r-project.org/src/contrib/Archive/WGCNA/
Cytoscape v3.9.0	Shannon et al., 2003 ⁷⁷	https://github.com/cytoscape/cytoscape/releases/3.9.0/
R v4.1.2	R Core Team ⁷⁸	https://www.r-project.org/
TO-GCN	Chang et al. ⁷⁹	https://github.com/petitmingchang/TO-GCN
Other		
DNBSEQ-T7RS sequencer	Beijing Genomics Institute (BGI)	N/A
DNBSEQ-T10 sequencer	Beijing Genomics Institute (BGI)	N/A

EXPERIMENTAL MODEL AND STUDY PARTICIPANT DETAILS**Plant material and growth condition**

To generate a comprehensive atlas of *Arabidopsis thaliana* at single-cell resolution, we used Columbia-0 (Col-0) ecotype for single-nucleic RNA-Seq and further experimental validation in this study. All the selected mutants were purchased from the AraShare (<https://www.arashare.cn/index/>). Seeds were surface-sterilized and plated on Murashige & Skoog (MS) medium (4.3 g/L MS salts, 1% sucrose, pH 5.7–5.8, and 8 g/L agar). The plates were then stored for 4 d at 4 °C before exposing to white light. Six days after germination, all the seedlings were transplanted into trays with nutrient soil and cultivated in a plant growth chamber at 22 °C under long-day condition (16 h light and 8 h dark cycles) with normal maintenance.

METHOD DETAILS**Plant materials preparation**

A total of 20 tissues (T1–T20) were collected from vegetative growth to reproductive growth. T1–T2: whole root from two stages of seedling (6d and 11d after germination); T3: shoot at 6d (including cotyledon, SAM and leaf primordia); T4: stem (whole stem including apical, middle and basal regions) at 42d; T5: cauline leaf at 42d; T6–T11: six stages of the second pair of true leaves from expansion to senescence (as shown by arrows); T12–T14: three stages of flowers (flower bud to fully opened flowers) at 49d; T15–T20: six successive timepoints of siliques (0 to 5d after anthesis with 1 day interval) (Figure 1A; Table S1). A detailed sampling strategy for 20 tissues was provided in the CNGB database (https://db.cngb.org/codeplot/datasets/Arabidopsis_Cell_Atlas). To facilitate the quantification of leaf senescence, the third and fourth rosette leaves at S4 were physically dissected into three fragments (base, middle and tip). For each sample, materials (~1 gram) were frozen immediately in liquid nitrogen and stored at -80 °C for nucleus isolation.

Single nucleus isolation

Nucleus isolation was prepared as described previously.¹⁰ The frozen materials were placed in 3 ml of Nuclear Isolation Buffer A (NIBA:0.8 M sucrose, 10 mM MgCl₂, 25 mM Tris-HCl (pH 8.0), 0.1 mM DTT, 0.4 U/μl RNase inhibitor and 0.1 mM PMSF) at 4 °C. The nuclei were harvested by chopping in NIBA at 4 °C. The mixture was subsequently filtered through 40 μm, 30 μm strainer and rinsed with 7 ml of NIBA, and then incubated for 10 minutes at 4 °C. Afterward, nuclei were centrifuged at 50 g for 5 min at 4 °C, the pellet was then removed and the supernatant was centrifuged at 2000 g for 10 min at 4 °C. The pellet was resuspended in 1ml Buffer B (0.4 M sucrose, 10 mM MgCl₂, 25 mM Tris-HCl (pH8.0), 0.2 U/μl RNase inhibitor, 0.1 mM PMSF, 1% Triton X-100). Percoll gradients were prepared on ice, i.e., 1 volume 75% percoll was added to tube, followed by 1ml 25% percoll. The nuclei suspension was then centrifuged at 3000g for 15min at 4 °C. The middle layer containing most of nuclei was transferred to a new tube and then washed with 5 volumes of Buffer B, and recovered by centrifuging at 1800g 10min at 4 °C. The nuclei pellet was resuspended in cell suspension buffer (CRB). The nuclei activity and concentration were measured by DAPI staining and hemocytometer, respectively.

Single-nucleus transcriptome sequencing (snRNA-seq) and data processing

Obtained single-nucleus suspensions were used for library preparation according to the DNBelab C Series Single-Cell Library Prep Set (MGI, 1000021082) as previously described.¹¹ The concentration of DNA library was measured by Qubit (Invitrogen). Libraries were sequenced by DNBSEQ-T7RS. The raw sequencing reads were filtered and demultiplexed by PISA (Version 1.1.0) (<https://github.com/shiquan/PISA>), and aligned to the TAIR10 reference genome using STAR (version 2.7.4a)⁶⁴ with default parameters. Then we obtained the raw matrix of Cell-gene UMI count by using PISA. The contamination fractions were removed by SoupX (v1.4.8)⁶⁵ with default settings to reduce the ambient RNA noise.

Quality control and unsupervised clustering

Unsupervised clustering of single cells was performed using Seurat R Package (version 3.2.1)⁶⁶ with the above modified matrix as input. Before clustering the cells, we preprocessed the data of each sample as following steps. First, cells with detected genes less than 200 or genes expressed in less than three cells were removed. To obtain more reliable data, we further filtered cells with more rigorous criteria, i.e., cells with less than 500 genes or more than 5% of organelle genes (chloroplast genes and mitochondria genes) were excluded. Then, the retained matrix was normalized using “NormalizeData” function with a global-scaling normalization method (normalization.method = “LogNormalize”) in Seurat, in which the read counts of each gene in a given cell were divided by the total valid read counts of that cell and then multiplied by the scale factor (scale.factor=10,000) before natural-log transformed. After that, highly variable genes (HVGs) were calculated using the function “FindVariableGenes” (selection.method= “vst”, nfeatures = 3000). To avoid the dominant effect of highly-expressed genes during analyses, a linear transformation was applied to scale the expression data using the “ScaleData” function, followed by the linear dimensional reduction using the function “RunPCA”. Finally, a K-nearest neighbor (KNN) graph-based approach implemented in functions “FindNeighbors” and “FindClusters” was employed to cluster all the retained cells into groups. Cell clustering results were visualized using both uniform manifold approximation and projection (UMAP). The DoubletFinder R package⁶⁷ was imported to predicted the possible doublet cells of each tissue and remove the doublet cells of the data before subsequent analysis.

Then, we merged different samples of each tissue and corrected the batch effect using harmony⁶⁸ with parameters dims.use set to 50 and lambda set to 1. For eliminating the effect of cell cycle genes, the cell cycle score of each cell was calculated and regressed out by the function of “CellCycleScoring” in Seurat during data scaling. Finally, the dimension reduction and clustering were conducted by harmony package for all the 20 tissues and for multiple samples collected from the same organs to generate a comprehensive transcriptome atlas.

Identification of cluster-specific differentially expressed genes

To define feature genes for each cell cluster, differentially expressed genes (DEGs) between each cell cluster and all other cell clusters were detected using “FindAllMarkers” function through non-parametric Wilcoxon Rank Sum test with only.pos = “TRUE”, logfc.threshold = 0.25 and min.pct = 0.25. The logfc.threshold parameter is the cutoff of expression fold change to test whether a gene was identified as differentially expressed in a certain cell cluster. The min.pct is the minimum percentage of a potential DEG expressed in all the cells.

Cell type annotation

To annotate the cell types for all the clusters retrieved in each tissue, known marker genes of different organs were collected from previous gene function reports and recent single-cell studies (Table S1). The cell type for each cluster was first manually defined using well-known marker genes that included in the list of cluster-enriched genes (Figures S1 and S2A–S2T; Table S1). For some clusters that lack well-known marker support, we used cluster-enriched genes in previous scRNA-seq studies to assist the annotation. Certain cell types captured at a single stage of an organ were underrepresented, making them challenging to cluster and identify in individual tissue samples. To address this, we identified these cell types by isolating them within clusters corresponding to the specific cell type in the integrated dataset across multiple stages of the organ.

Considering the advantage of single-nucleus data to reflect transcriptional diversity among different clusters within single cell type, we kept multiple clusters in a cell type separated following a majority of previously published studies (Column H in Table S1).

A description of cell type annotation for each main organ was provided in the CNGB database (https://db.cngb.org/codeplot/datasets/Arabidopsis_Cell_Atlas).

Correlation estimation between different cell types or tissues

To calculate the correlations between different cell types or same cell types from different tissues, we first calculated the average expression of each cell type with the function of “AverageExpression”. The average gene expression levels in these pseudo-bulked RNA-seq data of each cell type or tissue were then used for the calculation of Pearson’s correlations.

Spatial transcriptomes generated by Stereo-seq

Stems of plants at stage 5 (42 days after germination) were collected for Stereo-seq following the previously reported standard protocol V1.1 with some minor modifications.¹⁸ The materials were embedded in cryomolds that were pre-filled with OCT (SAKURA) and frozen on dry ice to prepare frozen blocks. The tissue blocks were acclimated at -20 °C for 30 min and cross sectioned at 10 µm thickness (Leika, CM1950). Sections were mounted onto a 1 cm x 1 cm Stereo-chip, incubated at 37 °C for 2 minutes, and then fixed in methanol at -20 °C for 40 minutes before imaging. The tissue on the chip was stained with the assay reagent from the Qubit ssDNA Assay Kit (Invitrogen) and used for imaging to get the tissue position with Motic PA53 Scanner. Tissue sections were permeabilized in 0.1% PR enzyme in 0.01 M HCl buffer (pH= 2) at 37 °C for 12 minutes, and incubated overnight at 42 °C for reverse transcription and cDNA synthesis. Afterward, the chip was treated with Exonuclease I (NEB, M0293L) for 1 hour at 37 °C and then was placed in cDNA release buffer for 3 hours. The cDNA products were used for DNB generation and finally sequenced (paired-end 50 bp or paired-end 100 bp) on a MGI DNBSEQ-T10 sequencer.

Spatial transcriptomic analyses

Spatial transcriptomic data was processed as described in the previously reported Stereo-seq method.¹⁸ Briefly, the sequenced reads were aligned to the TAIR10 reference genome to create expression profile matrix using STAR (version 2.7.4a)⁶⁴ with default parameters. Then the bins40-gene matrix was created, normalized and scaled by the function of ‘SCTtransform’ and integrated with snRNA-seq data of stem by the function of ‘TransferData’ in Seurat package (version 3.2.1) with default parameters.

Gene Ontology term enrichment analysis

To predict the potential biological functions of each cell cluster, cluster-specific DEGs generated in the above steps were used to perform Gene Ontology (GO) term enrichment analysis. This step was achieved by utilizing the ‘enrichGO’ function with the Benjamini-and-Hochberg (BH) method (pAdjustMethod = “BH”) implemented in clusterProfiler R package.⁶⁹ The GO annotation for cluster-specific DEGs were retrieved from the ‘org.At.tair.db’ dataset (OrgDb = org.At.tair.db) implemented in the DOSE R package,⁷⁰ in which the GO distribution was used as the background for GO over-representation analysis. GO terms with adjusted P-value lower than 0.05 (pvalueCutoff = 0.05) were considered significantly over-represented.

To elucidate potential triggers of putative early senescent cells, DEGs were identified between cells with top 5% SAG-index and cells with intermediate SAG-index (45–55%) in visibly green S3 leaves. GO enrichment was then performed with agriGO (v2, <http://systemsbiology.cau.edu.cn/agriGOv2/>) for epidermis, mesophyll and vascular cells, respectively.

Pseudotime analysis

Considering the suitability of estimating cell states with high heterogeneity and pseudotime across multiple stages (Figures S4W–S4Z), the trajectory analyses of six-stage leaf cells and pollen cells from three-stage flowers in this study were conducted by employing implemented functions in Monocle2 (version 2.18.0).⁷¹ For the root organs that showed minor heterogeneity, we used Monocle3 (version 1.0.0)⁷² for pseudotime analysis, a beta version that requires manual determination of roots during analysis. The normalized gene expression data was extracted from specific organs or cell types and reclustered by Seurat. Then the DEGs that identified by Seurat were used as the variable genes to perform pseudotime analysis. The pseudotime analysis using Monocle 2 starts with the data dimension reduction using function “reduceDimension”, followed by ordering the cells according to their pseudotime by function “orderCells”. Cells from the six-stage leaves were then grouped by equally dividing the pseudotime into 10 bins (T0–T9) for downstream analysis. For pseudotime analysis with Monocle 3, representative genes were selected for dimension reduction, followed by learning the trajectories of cells transitioning from one state to another based on the distance from a manually selected root to each cell along the trajectory.

Organ- and cell-type-enriched transcription factors analysis

To estimate the regulation similarities and divergences among different organs and cell types, the average expression levels of all expressed transcription factors (summed >1) in the five major organs were calculated for the five major cell types (epidermis, mesophyll, xylem, CC and PP) after integrative normalization across organs. Then the normalized expressions were analyzed as pseudotime-ordered data using TO-GCN,⁷³ with the average gene expressions of the same cell type in all the five organs as control. Highly expressed transcription factors were clustered at either organ or cell-type levels. The numbers of inter-organ transcription factor interactions were counted for each cell-type and used to represent the inter-organ regulation similarities.

Leaf SAG-index and YAG-index modeling and application in bulked RNA-seq data

To estimate the senescence state of cell, we proposed two indexes, SAG-index and YAG-index, to comprehensively represent the cell state at single-cell level. Firstly, genes that highly expressed at S5 and/or S6 in epidermis, mesophyll and vascular cells were extracted as candidate leaf senescence-associated genes (SAGs). The resulting 6,391 genes shared in three major cell types were then compared with previously reported 3,855 SAGs,³¹ leading to 1,856 overlapped core SAGs. Then the relative expression level of each gene in each cell was divided by its average expression level in all cells at S5 and S6. Eventually, the average of relative expression level of all core SAGs in each cell was defined as SAG-index.

Similarly, to calculate the YAG-index, genes that highly expressed at S1 in all the three major cell types were extracted as candidate youth associated genes (YAGs). The relative expression levels of the shared 1,875 YAGs were then divided by the corresponding average expression levels in S1. The average of relative expression levels of all YAGs were designated as YAG-index for each cell. The calculation of SAG-index and YAG-index is given as following formula.

$$\text{SAG-} / \text{YAG-index} = \text{mean} \left(\sum_{i=1}^{i=N} \frac{X}{M} \right)$$

X is the normalized gene expression level of one SAG or YAG in each cell, i is the number of the core SAGs or YAGs. For calculation of SAG-index, M is the average expression levels of gene i in S5 and S6. For calculation of YAGs-index, M is the average expression level of gene i in S1.

To estimate the validity of SAG-index and YAG-index, we applied SAG-index and YAG-index to bulked RNA-seq data of multiple organs and various stress conditions. The bulked RNA-seq data were downloaded from the NCBI Sequence Read Archive (SRA) (Table S2). The clean data was aligned to the TAIR10 reference genome (v48) using HISAT2 (version 2.2.1)^{73,74} with parameters '-5 10 -3 5'. StringTie (v1.3.6) was imported to estimate the abundance of annotated genes in reference genome.⁷⁵ Only samples with high Pearson's correlations (≥ 0.95) with other repeats were included in analyses. For the application of SAG-index and YAG-index in estimating leaf development and senescence in *Populus*, two bulked RNA-seq datasets using successive developmental sampling strategy were downloaded and reanalyzed.^{80,81} Genes showed relatively higher expressions at early and late stages were extracted, and only genes showed high similarity in protein sequences with the core SAGs and YAGs we identified in *Arabidopsis* were used for calculation of SAG-index and YAG-index as the above formula.

To align the senescent state of cells to SAG-index, the cells were firstly sorted by SAG-index, and then the accumulated expressions of marker genes (*SAG12*, *SAG13*, and *RBCS1A*) were calculated and normalized by the maximum expression levels for each gene.

Weighted gene coexpression network analysis (WGCNA)

To fully identify the genes related to leaf senescence, weighted gene coexpression network analysis (WGCNA) was performed with the average expression levels (FPKM) of all expressed genes in epidermis, mesophyll and vascular cells at each stage using the functions in R package WGCNA (v1.68).⁷⁶ The soft threshold (power/ β) was determined with optimal scale-free topology model fit signed $R^2 > 0.85$ and mean connectivity ≤ 100 . The coexpression gene module eigengenes (MEs) were identified with the following parameters: deepSplit level 2, minModuleSize of 50, and tree mergeCutHeight of 0.30. MEs with strong correlations ($R^2 > 0.5$) with SAG-index or YAG-index were defined as candidate modules related to leaf senescence. To further estimate the correlations between each gene in these candidate modules and identify promising master genes associated with leaf senescence, we proposed a coexpression score based on the Gene Significance (GS) values and the interactions with known promoting-/delaying senescence genes. The GS values are the correlation between each gene and SAG-index. The interactions of each gene with the functional known promoting or delaying senescence genes were firstly ranked by the weight, and only the interactions with $>95\%$ weight (kME) was counted. Then the coexpression scores were calculated by multiplying GS values and \log_2 transformed interactions. The gene networks with known functional SAGs in these modules were extracted and visualized with Cytoscape (v3.9.0)⁷⁷. The node sizes were determined by the $-\log_{10}$ transformed p-values between each gene and SAG-index. All the nodes were colored based on coexpression score. The known functional SAGs and selected hub genes were classified based on their functions.

Marker line generation and confocal observation

To generate the *RPGE2pro::RPGE2-GFP* expressing vector, a 2,736bp genomic fragment of *RPGE2* locus containing its native promoter (1,909bp) and coding region (827bp) was amplified by PCR from genomic DNA and inserted into the pQG110-35S-GFP vector⁸² using *Pst*I and *Sal*I restriction sites to generate pQG110-RPGE2pro-RPGE2-GFP plasmid. The plasmids were transformed into *Agrobacterium tumefaciens* strain GV3101 and then integrated into *Arabidopsis* Col-0 using the floral dip method. Primers used for molecular cloning are listed in Table S13. For GFP observation of *RPGE2pro::RPGE2-GFP/Col-0* plants, intact S3-stage leaf was imaged using a Zeiss LSM880 confocal microscope (Carl Zeiss). GFP signal was activated with a 488 nm argon laser, and the emission were collected between 493 and 564 nm.

Age-dependent leaf senescence assays

Age-dependent leaf senescence was evaluated as described previously.⁸³ The second pair of rosette leaves of individual plants at the indicated developmental stages were detached, photographed for visual inspection of leaf color, and used to assess chlorophyll

content. For chlorophyll measurement, detached second pair of rosette leaves were incubated in absolute ethanol in the dark overnight. Absorbance was measured at 645 and 663 nm, and the chlorophyll contents were calculated as previously described.⁸⁴

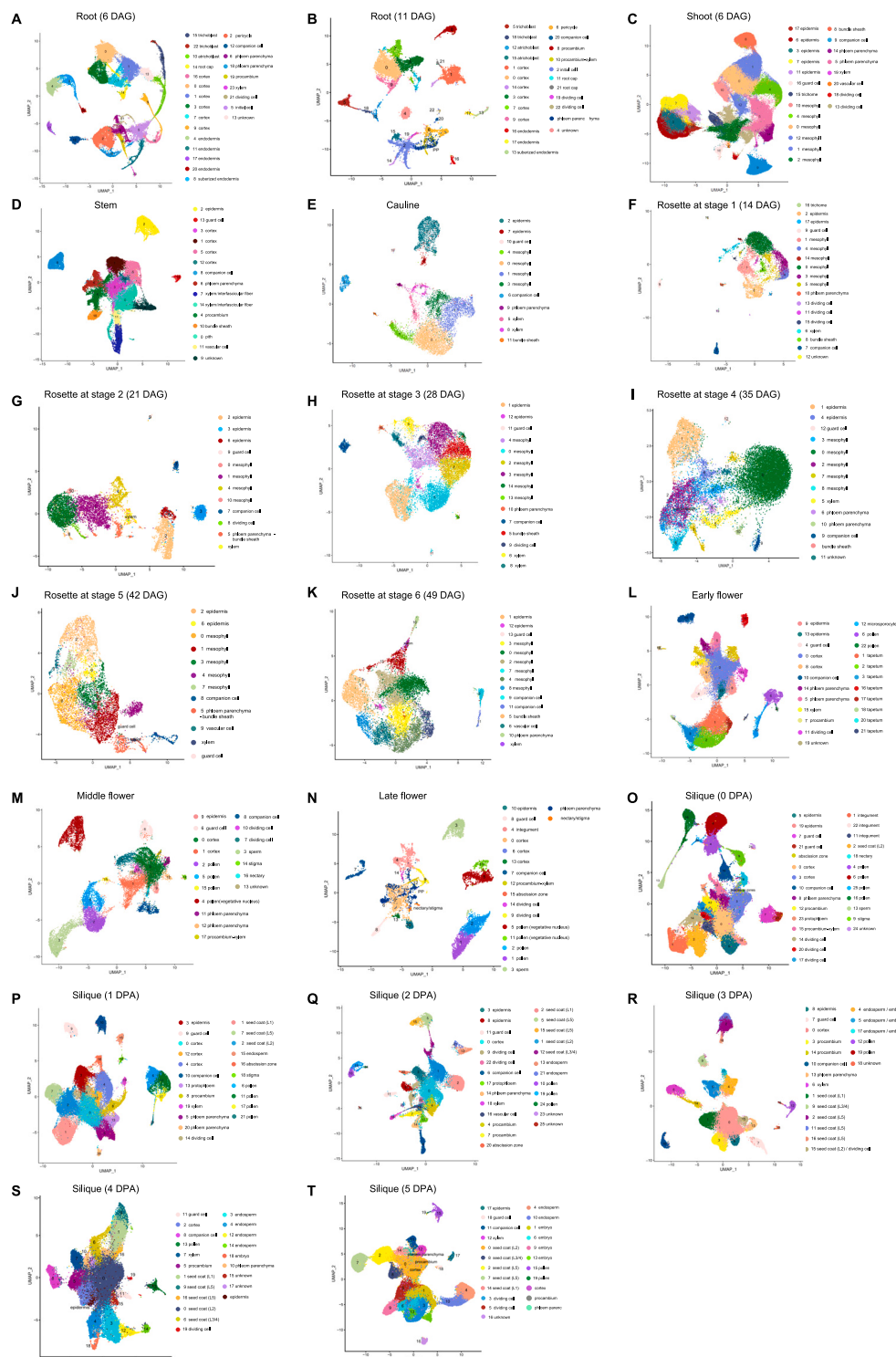
RNA extraction and quantitative real-time PCR analysis

The second pair of rosette leaves of individual plants were detached to estimate the relative expression levels of SAG12, SAG13 and RBCS1A by real-time PCR analysis. Total RNA from leaves was extracted using plant RNA kits (ER301; TransGen Biotech, Beijing, China), and cDNA was synthesized using a cDNA synthesis kit (AT341; TransGen Biotech). Quantitative reverse transcription polymerase chain reaction (RT-qPCR) analysis was performed to determine the gene expression levels using a RT-qPCR kit (W812014; Welab Biotech, Beijing, China), and then the relative mRNA quantities were calculated from the average values using the $\Delta\Delta C_T$ method.⁸⁵ *Arabidopsis ubiquitin-Conjugating Enzyme 21 (UBC21)* gene was used as an internal reference to normalize the expression value in each sample. Three replicates were examined for each sample, and the relatively mean expression levels were shown after normalization based on the maximum expressions for each gene. All the primers used for RT-qPCR were listed in [STAR methods](#).

QUANTIFICATION AND STATISTICAL ANALYSIS

The Student's *t*-test was used for statistical analysis to estimate the chlorophyll contents ([Figures 4G and S5G](#)) and SAG-/YAG-index distributions in root samples (6d and 11d, [Figure S4N](#)), assuming that the samples showed no significant differences. For the chlorophyll contents, four biological replicates were used for each sample and measured by Mean \pm SD. The *t*-test statistical significances were indicated with a-g in [Figure 4G](#) and a-d in [Figure S5G](#), respectively. For the SAG-/YAG-index analysis in root samples, all the cells were included for calculating SAG-/YAG-index, with n=44,469 for 6d root and n=12,141 for 11d root, respectively. The *t*-test significances were indicated with asterisks (**<0.001).

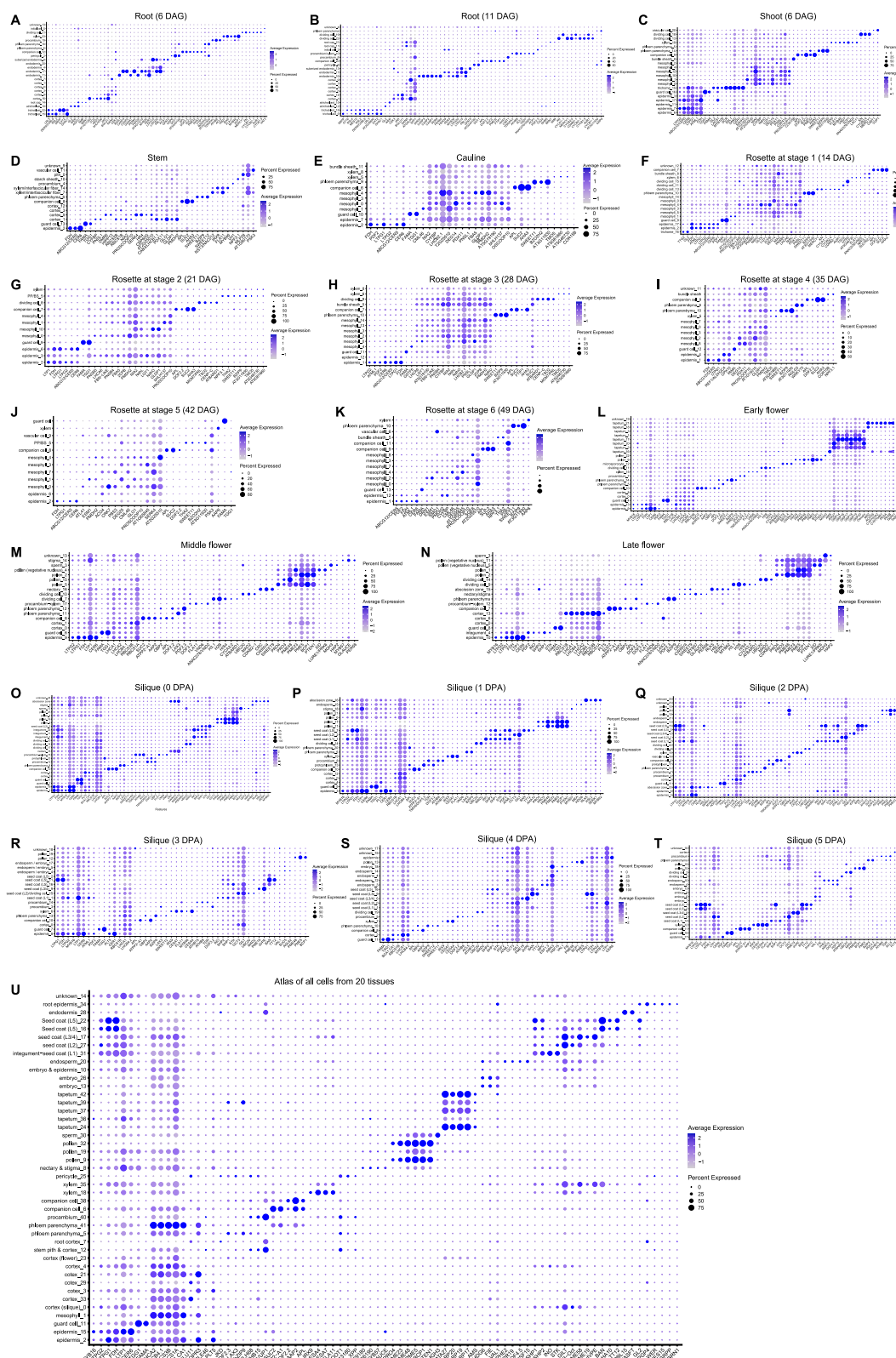
Supplemental figures



(legend on next page)

Figure S1. snRNA-seq profiling of all tissues, related to Figure 1

UMAP clustering and annotation of cell types in single tissue, including 6 DAG root (A), 11 DAG root (B), 6 DAG shoot (C), 42 DAG stem (D), 42 DAG caulin (E), rosette at stage 1–6 (14 DAG, 21 DAG, 28 DAG, 35 DAG, 42 DAG, 49 DAG; F–K), early flower (L), middle flower (M), late flower (N), and 0–5 DPA siliques (O–T). DAG, days after germination. DPA, days post anthesis.



(legend on next page)

Figure S2. Dot plot of marker genes of all tissues in the indicated cell types, related to Figure 1

The tissues include 6 DAG root (A), 11 DAG root (B), 6 DAG shoot (C), 42 DAG stem (D), 42 DAG caulin (E), rosette at stage 1–6 (14 DAG, 21 DAG, 28 DAG, 35 DAG, 42 DAG, and 49 DAG; F–K), early flower (L), middle flower (M), late flower (N), 0–5 DPA siliques (O–T), and atlas using all cells from 20 tissues. DAG, days after germination. DPA, days post anthesis. The color indicates the scaled average expression, while the size of the circles represents the ratio of expression cells in each cluster.

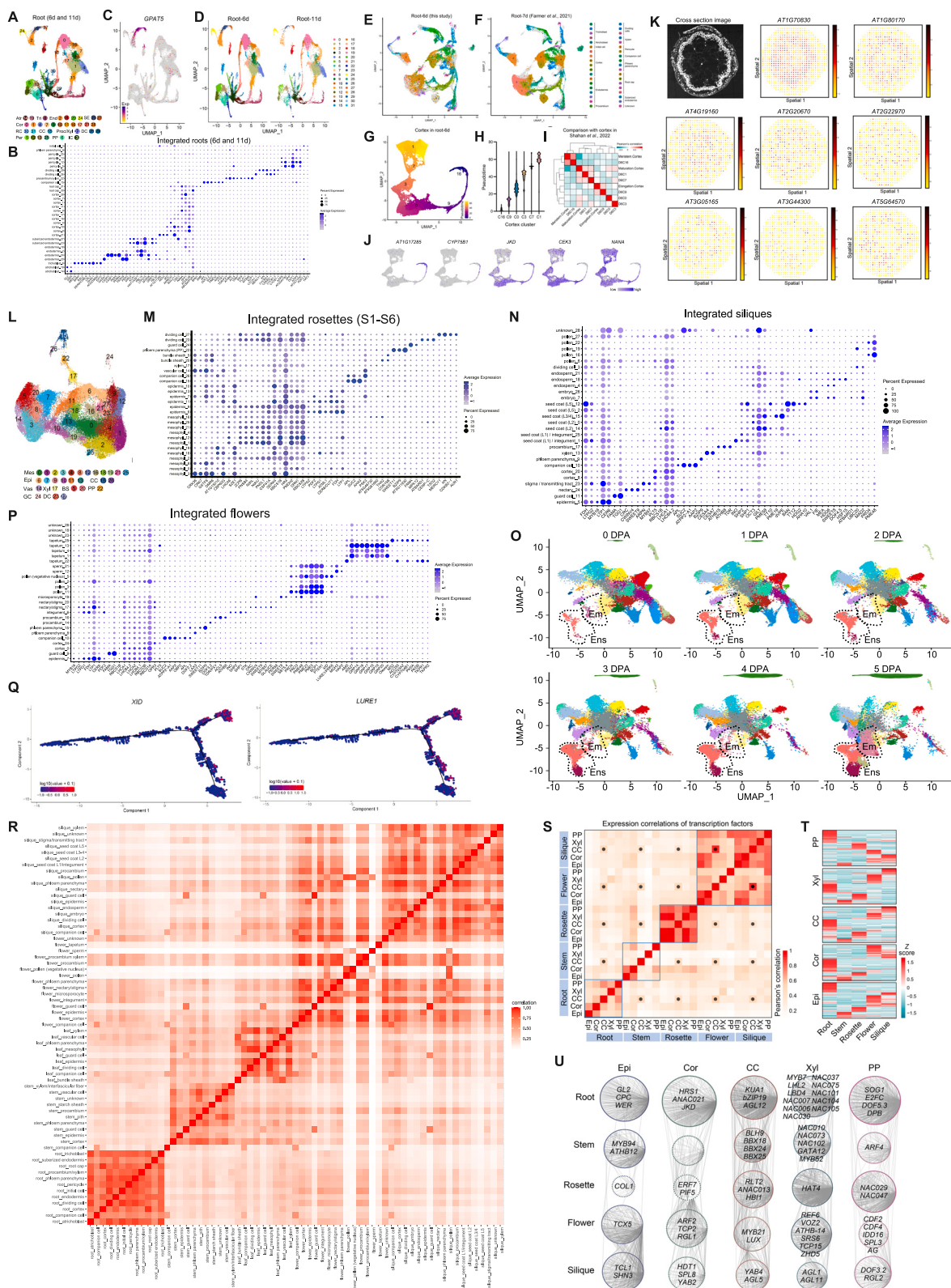
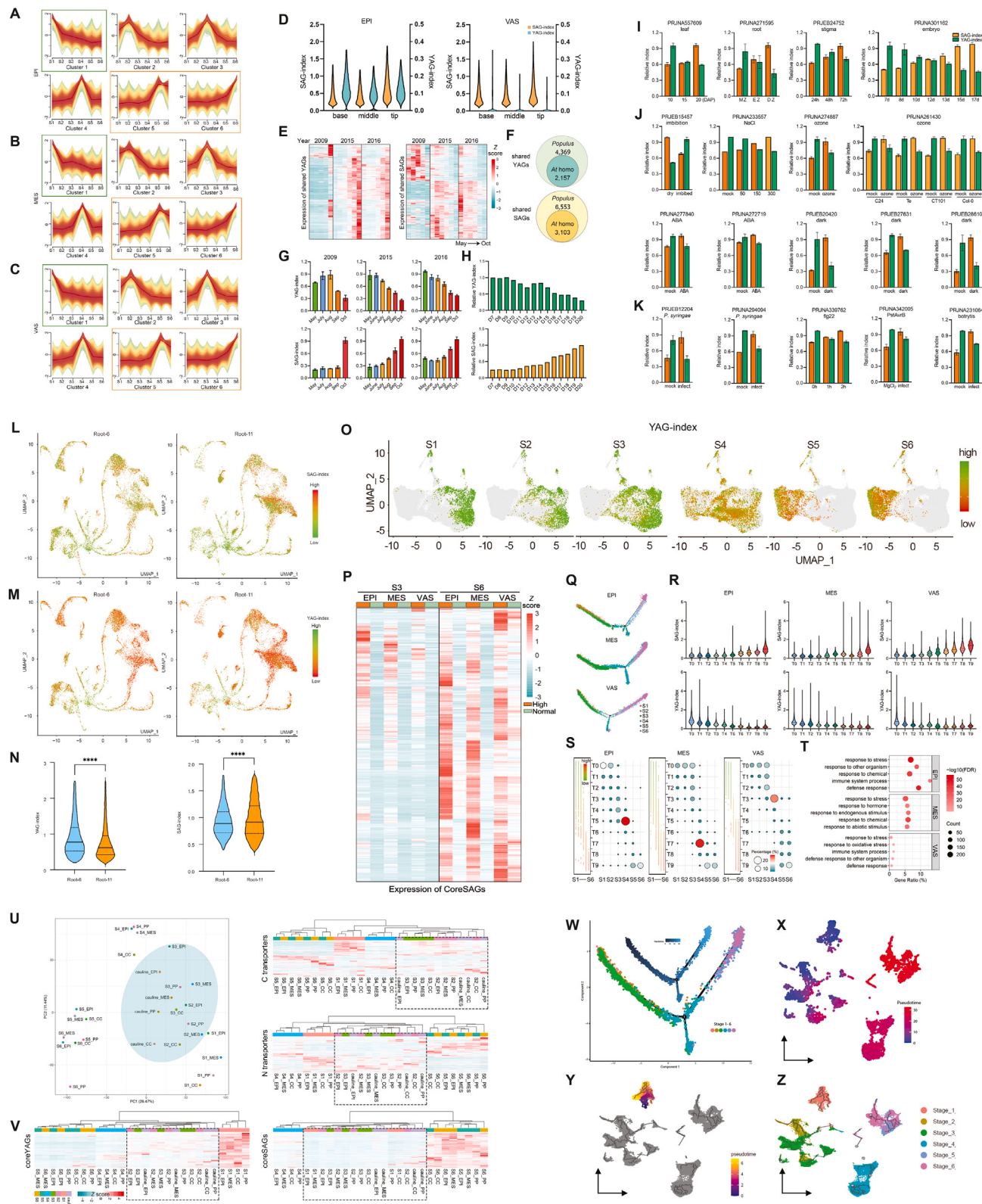


Figure S3. Intra-organ integration and cross-organ comparison, related to Figure 2

- (A) Integrated UMAP and annotation of 6-day and 11-day roots.
(B) Expression of marker genes for cluster annotation.
(C) Expression of suberized endodermis marker gene *GPAT5*.
(D) Splitted UMAP plots of 6-day and 11-day roots. The clusters are consistent with (A).
(E and F) Cell clustering comparison of 6-day root in this study and 7-day root from Farmer et al.¹² based on an integrated dataset from 57,775 nuclei. The gray background showed the integrated cell clustering. Cells of 6-day roots in this study are indicated by colored dots in (E). Cells of 7-day roots from Farmer et al.¹² are showed by colored dots in (F).
(G) Pseudotime trajectory analysis of the six cortex clusters in 6-day root.
(H) Statistics of pseudotime for each cortex cluster.
(I) Expression similarities of the six cortex clusters in this study with the cortex data from Shahan et al.¹⁶
(J) Dynamic expressions of five cortex marker genes with spatial information along pseudotime.
(K) Expression patterns of *de novo* identified stem pith marker genes in the Stereo-seq transcriptome data.
(L) Integrated UMAP and annotation of the six-stage rosette.
(M) Dotplot of marker genes for each cluster in the six-stage rosette.
(N) Dotplot of marker genes for each cluster.
(O) Endosperm (Ens) and embryo (Em) development in siliques along sampling stages.
(P) Dotplot of marker genes for each cluster of integrated flowers.
(Q) Expression patterns of VN marker genes XID and LURE1 along pseudotime trajectory.
(R) Expression similarities of all identified cell types from root, stem, rosette, flower, and silique. Pearson's correlations were used to estimate the expression similarities among all the cell types and clusters in the five major organs.
(S) Expression similarities of TFs for EPI, cortex (Cor), companion cell (CC), xylem (Xyl), and phloem parenchyma (PP) in the five major organs.
(T) Heatmap of TFs that showed distinct expression patterns among the five major organs.
(U) Cell-type specific enrichment of TFs in the five major organs. Known TFs that function in specific cell types were marked for each cell type in the five major organs.
- See abbreviations for cell types in [Figure 2](#).



(legend on next page)

Figure S4. Quantification of leaf senescence at single-cell level by YAG-index and SAG-index, related to Figure 3

- (A–C) Selection of SAGs and YAGs in EPI (A), mesophyll (MES) (B), and VAS (C) cells of rosette leaves based on gene expression patterns along sampling stages. Clusters marked with green and orange boxes are genes with relatively higher expressions at early (S1) or late stages (S5–S6) in the three major cell types, respectively.
- (D) Statistics of SAG-index and YAG-index in EPI and VAS cells located in base, middle, and tip segments of S4 rosette leaf.
- (E) Expression patterns of shared YAGs and SAGs in the 3-year *Populus* leaves that collected from May to October (NCBI SRA accession PRJNA597006⁷⁵).
- (F) Identification of YAGs and SAGs homologs between *Populus* and *Arabidopsis* based on protein similarities.
- (G) Statistics of relative YAG-index and SAG-index that calculated based on homologous YAGs and SAGs between *Populus* and *Arabidopsis*.
- (H) Relative YAG-index and SAG-index in *Populus tomentosa* leaves from day 7 to day 20 after emergence.⁷⁶
- (I–K) SAG-index and YAG-index distribution in bulked RNA-seq data of among different tissues (I), under abiotic stresses (J), and under biotic stresses (K).
- (L and M) Distributions of SAG-index and YAG-index in 6-day and 11-day roots.
- (N) Comparison of SAG-index and YAG-index in 6-day and 11-day roots. Data = mean ± SD, $n = 44,469$ for 6-day root, $n = 12,141$ for 11-day root. The t test statistical significances were indicated with asterisks (**<0.001).
- (O) Dynamic changes of YAG-index in the six stages of rosette leaves.
- (P) Expression of coreSAGs in cells with relatively high SAG-index at S3.
- (Q) Pseudotime trajectories of EPI, MES, and VAS cells.
- (R) Statistics of SAG-index and YAG-index along pseudotime bins. The pseudotime of each cell type was equally divided into 10 bins (T0–T9).
- (S) Statistics of cell origins along pseudotime bins. The percentages were calculated by dividing the total cell numbers for each cell type.
- (T) GO enrichment analysis of cells at the turning points at S4 for each cell type.
- (U) PCA of global expressions between the 42-day cauline leaf and the six-stage rosette leaves (S1–S6).
- (V) Clustering of expressed carbon, nitrogen transporters, coreYAGs, and coreSAGs between the 42-day cauline leaf and the six-stage rosette leaves.
- (W) The development trajectory of cells from six-stage leaves analyzed using Monocle 2.
- (X) UMAP heatmap showing the pseudotime value of cells from six-stage leaves using Monocle 2.
- (Y) UMAP heatmap showing the pseudotime value of cells from six-stage leaves using Monocle 3.
- (Z) UMAP showing the stage of cells plotted in the (Y).

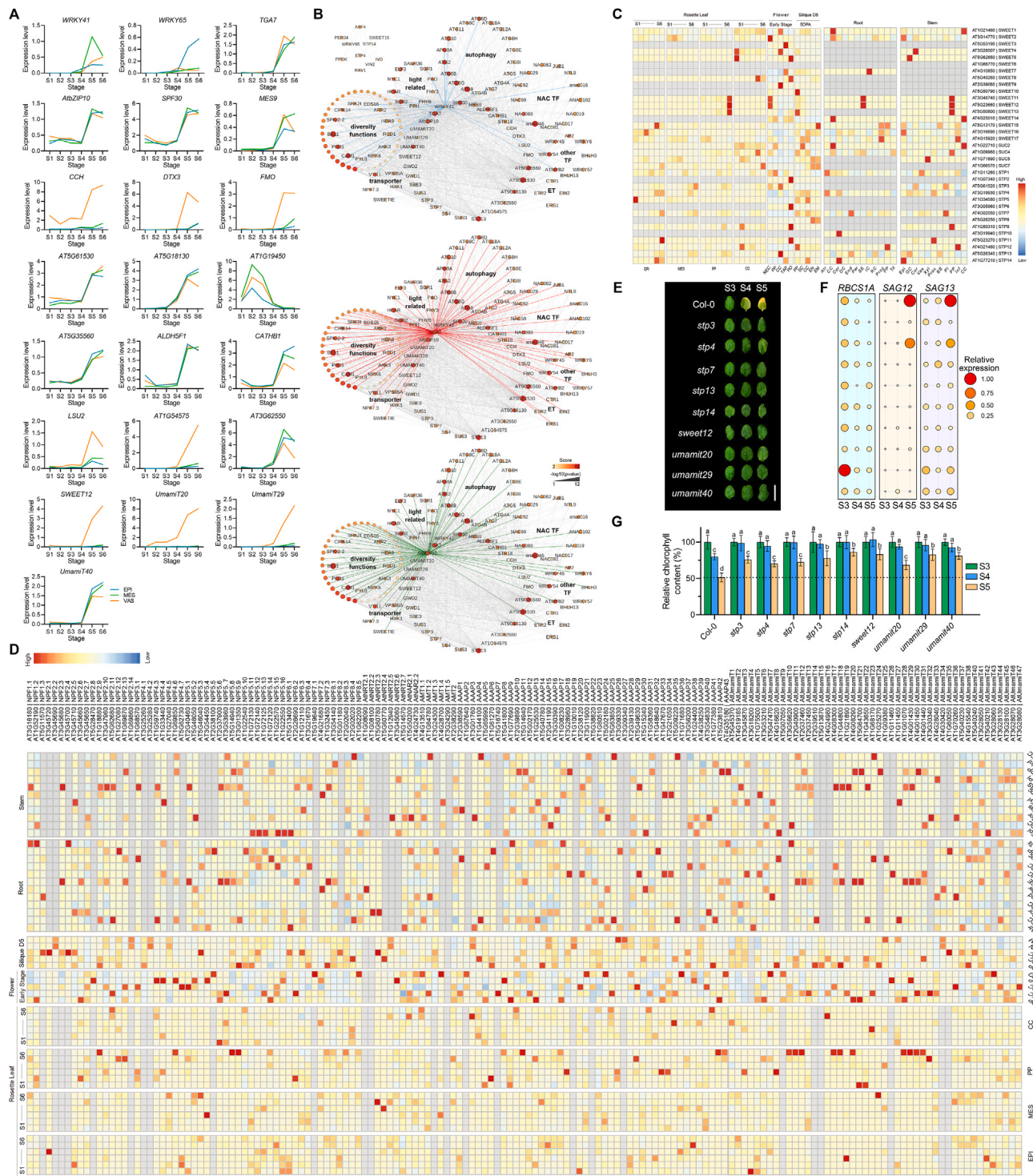


Figure S5. Expression patterns of selected promising hub SAGs and C/N transporters in six-stage leaves and sink organs, related to Figures 4 and 5

(A) Expression patterns of the selected promising hub genes in EPI, MES, and VAS cells along leaf sampling stages.

(B) Co-expression patterns of WRKY41, WRKY65, TGA7, and AtbZIP10 with the 160 functional validated SAGs

(C) and (D) Heatmap of cell-type-specific and temporal expression patterns of major carbon (C) and nitrogen (D) transporter genes in leaves (S1–S6), developing flower (early stage), and silique (5 DPA).

(legend continued on next page)

-
- (E) Phenotypes of the fourth rosette leaves in mutants of selected C/N transporters at the indicated age. The wild-type Col-0 is used as control. Representative leaves were shown for each sample. Scale bar, 1 cm.
- (F) RT-qPCR analysis of *SAG1*, *SAG13*, and *RBCS1A* expression in the leaves shown in (E). Three replicates were examined for each sample, and the relatively mean expression levels were shown after normalization based on the maximum expressions for each gene (see [STAR Methods](#)).
- (G) Chlorophyll contents in the leaves shown in (E). Data = mean \pm SD, $n = 4$. The t test statistical significances were indicated with a-d. DPA, days post anthesis. See abbreviations for cell types in [Figure 2](#).